MRI Perfusion Measurements using Magnetic Susceptibility Effects: Calibration Approaches and Contrast Agent Quantification

Lind, Emelie

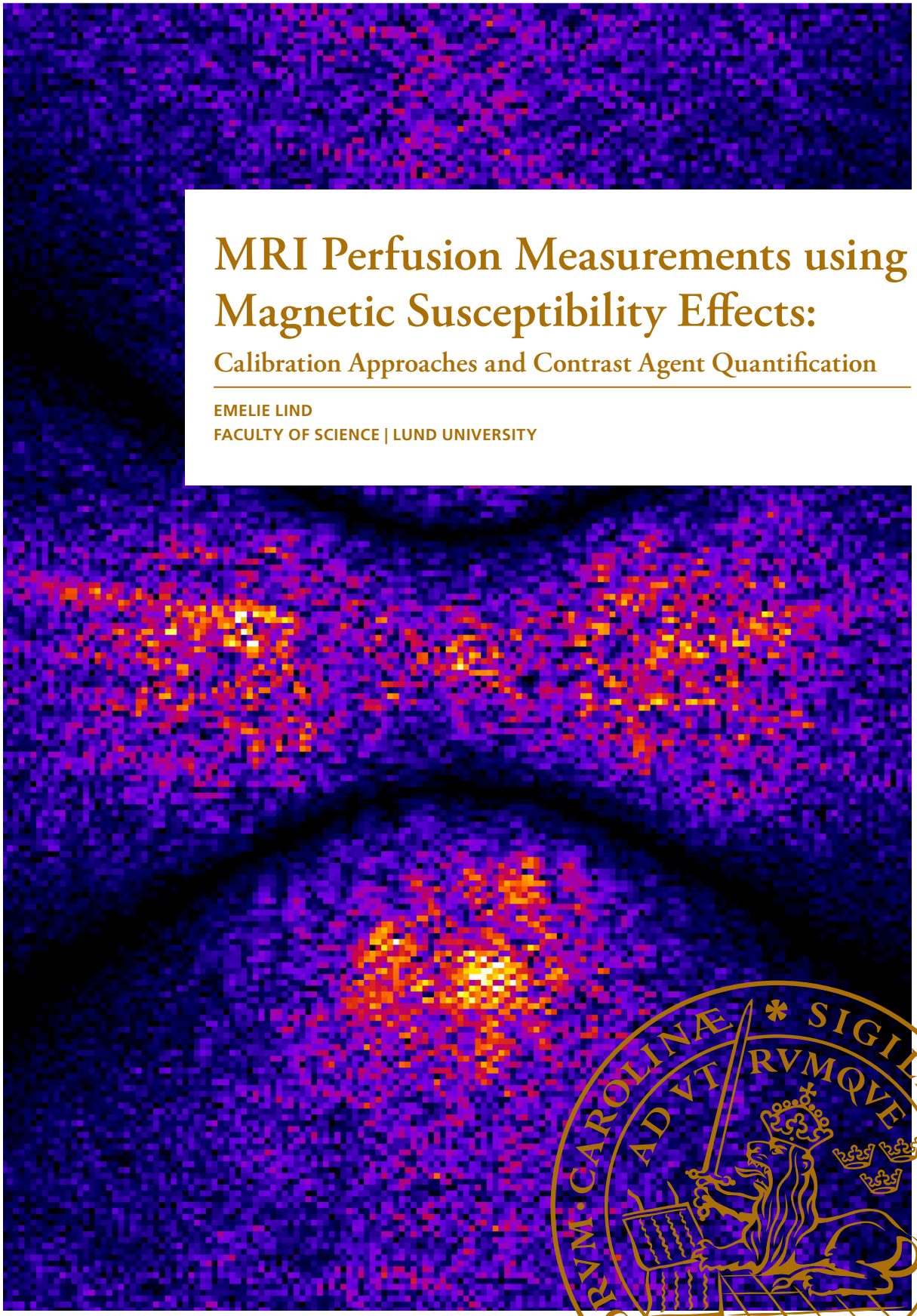

MRI Perfusion Measurements using Magnetic Susceptibility Effects:

Calibration Approaches and Contrast Agent Quantification

EMELIE LIND
FACULTY OF SCIENCE | LUND UNIVERSITY

MRI Perfusion Measurements using Magnetic Susceptibility Effects

MRI Perfusion Measurements using Magnetic Susceptibility Effects:

Calibration Approaches and Contrast Agent Quantification

Emelie Lind

LUND
UNIVERSITY

DOCTORAL DISSERTATION
by due permission of the Faculty of Science at Lund University in Sweden.
To be defended at Demonstration Room 10, Department of Medical Imaging and Physiology, Main Building, Level IV, Skåne University Hospital in Lund on Friday the 1st of March 2019 at 9:00 am

Faculty opponent
Kyrre Eeg Emblem
Department of Diagnostic Physics
Oslo University Hospital

Organisation	Document name
LUND UNIVERSITY Department of Medical Radiation Physics	DOCTORAL THESIS
	Date of issue: 5 FEBRUARY 2019
Author EMELIE LIND	Sponsoring organisation

Title and subtitle: MRI PERFUSION MEASUREMENTS USING MAGNETIC SUSCEPTIBILITY EFFECTS: CALIBRATION APPROACHES AND CONTRAST AGENT QUANTIFICATION

Exchange of oxygen and nutrients between blood and tissue occurs at the capillary level of the blood system. The blood volume flow rate in the capillaries is often referred to as perfusion, and knowledge about perfusion provides important information about the function and viability of the tissue, for example, in patients with ischaemic stroke, cancer, and neurodegenerative diseases.

Dynamic susceptibility contrast magnetic resonance imaging (DSC–MRI) is the basic data collection approach used to obtain perfusion information from the studies reported in this doctoral thesis. The approach shows the advantage of providing estimates of not only brain perfusion, or cerebral blood flow (CBF), but also cerebral blood volume (CBV) and mean transit time (MTT). All of these parameters are required for a comprehensive description of microcirculation. When using standard implementations of DSC–MRI image acquisition and post-processing routines, the CBF and CBV values are often overestimated. In DSC–MRI, a contrast agent (CA) bolus is injected intravenously in an arm vein and is subsequently tracked by rapid imaging when passing through the brain. To calculate CBF, CBV, and MTT, CA concentration information from both tissue and blood is required. The main problem of DSC–MRI is estimating reliable CA concentration levels in tissue and artery simultaneously. Relatedly, if transverse relaxivity-based information is used, then the response to the CA, in terms of the change in relaxation rate, $\Delta R2^*$, differs between blood and tissue. Additionally, there is a non-linear dependence on CA concentration in whole blood. Another issue related to estimations of blood concentration is the practical difficulty of finding a voxel containing only blood, implying that the concentration time curve representing blood will be affected by the surrounding tissue, possibly influencing both the shape of the curve and the absolute levels of estimated concentrations.

One approach is to obtain CBV estimates with alternative methods, where contrast agent concentration is quantified using the longitudinal relaxation time, T1, or by using a special MRI pulse sequence designed to study the blood contribution to the MRI signal. The information from these additional CBV estimates is used to calibrate the conventional DSC–MRI data. This approach provided perfusion results with the expected absolute levels but showed moderate repeatability and low correlation with arterial spin labelling (ASL), used as a reference perfusion imaging method. Another study included in the context of this doctoral thesis dealt with the issue of partial-volume effects in the voxel selected to represent blood. By rescaling the area under the curve (AUC) of the concentration-versus-time curve measured in an artery (assumed to show the desired shape), with the AUC of a large vein, measured under circumstances more favourable for blood-data registration, CBF and CBV values were calibrated. This method aims primarily to correct for partial volume effects in the blood voxel (i.e. it does not directly address relaxivity issues). An observation of interest in this context was that absolute perfusion levels similar to what was expected from literature data were obtained. Furthermore, the repeatability was more promising using this approach, compared to the ones described above.

The phase of the MRI signal is related to the magnetic field strength, which, in turn, is related to the magnetic susceptibility. As the CA alters the magnetic susceptibility, it should, in principle, be possible to obtain information about CA concentration using MRI phase information. This approach was used in three of the studies described in this thesis, for calculation of perfusion-related parameters in relative and absolute terms. These studies indicated that information about (or related to) magnetic susceptibility is a promising method for estimating CA concentration, whereas a number of methodological issues still need to be resolved or further investigated. It was also shown that the shape of an arterial $\Delta R2^*$ curve, based on DSC–MRI data, displayed a shape similar to the corresponding curve obtained by using magnetic susceptibility information for assessment of concentration. Thus, the shape of a typical arterial blood concentration curve used in a standard DSC–MRI experiment can probably be regarded reasonably reliable. However, the AUC is likely to be underestimated because of partial-volume effects.

Key words: contrast agent, cerebral blood flow, cerebral blood volume, mean transit time, perfusion, dynamic susceptibility contrast MRI, magnetic susceptibility

Classification system and/or index terms (if any)

Supplementary bibliographical information	Language English
ISSN and key title	ISBN 978-91-7753-972-8 (print) 978-91-7753-973-5 (pdf)

Recipient's notes	Number of pages 181	Price
	Security classification	

Signature  Date 2019-01-21

MRI Perfusion Measurements using Magnetic Susceptibility Effects:

Calibration Approaches and Contrast Agent Quantification

Emelie Lind

Department of Medical Radiation Physics
Lund University

2019

LUND
UNIVERSITY

Main supervisor: Professor **Ronnie Wirestam**
Supervisors: Professor **Linda Knutsson** and Professor **Freddy Ståhlberg**

Cover photo shows a visualisation of k-space which corresponds to a susceptibility distribution in brain convolved with the dipole kernel

Funding information: The thesis work was financially supported by the Swedish Research Council, the Swedish Cancer Society, the Crafoord Foundation and Hjärnfonden

Department of Medical Radiation Physics
Faculty of Science
Lund University
SE-221 85 Lund Sweden

ISBN 978-91-7753-972-8 (print)
ISBN 978-91-7753-973-5 (pdf)

Printed in Sweden by Media–Tryck, Lund University
Lund 2019

Media-Tryck is an environmentally certified and ISO 14001 certified provider of printed material. Read more about our environmental work at www.mediatryck.lu.se

In the realm of ideas everything depends on enthusiasm… in the real world all rests on perseverance

- Johann Wolfgang von Goethe

Table of Contents

Abstract

Exchange of oxygen and nutrients between blood and tissue occurs at the capillary level of the blood system. The blood volume flow rate in the capillaries is often referred to as perfusion, and knowledge about perfusion provides important information about the function and viability of the tissue. Hence, perfusion measurements are valuable for diagnoses of patients with, for example, ischaemic stroke, cancer, and neurodegenerative diseases.

Using magnetic resonance imaging (MRI), perfusion measurements can be conducted without the need for ionizing radiation, which is especially important for children and patients who experience many repeated measurements over time. Dynamic susceptibility contrast MRI (DSC–MRI) is the basic data collection approach used to obtain perfusion information from the studies reported in this doctoral thesis. The approach shows the advantage of providing estimates of not only brain perfusion, or cerebral blood flow (CBF), but also of other perfusion-related parameters (i.e. cerebral blood volume (CBV) and mean transit time (MTT)). All of these parameters are required for a comprehensive description of microcirculation.

When using standard implementations of DSC–MRI image acquisition and post-processing routines, the CBF and CBV values are often overestimated. In DSC–MRI, a contrast agent bolus is injected intravenously in an arm vein and is subsequently tracked by rapid imaging when passing through the brain. Hence, a dynamic measurement needs to be conducted, and to calculate CBF, CBV, and MTT, contrast agent concentration information from both tissue and blood is required. The main problem of DSC–MRI is estimating reliable contrast agent concentration levels in tissue and artery simultaneously. Relatedly, if transverse relaxivity-based information is used, then the response to the contrast agent, in terms of the change in relaxation rate, $\Delta R2^*$, differs between blood and tissue. Additionally, there is a non-linear dependence on concentration in whole blood. Another issue related to estimations of blood concentration is the practical difficulty of finding a voxel containing only blood, implying that the concentration time curve representing blood will be affected by the surrounding tissue, possibly influencing both the shape of the curve and the absolute levels of estimated concentrations.

In this thesis, studies of both issues are reported. One approach is to obtain CBV estimates with two alternative methods, where contrast agent concentration is quantified using the longitudinal relaxation time, T1, or by using a special MRI pulse sequence designed to study the blood contribution to the MRI signal. The information from these additional CBV estimates was used to calibrate the conventional DSC–MRI data. This approach provided perfusion results with the

expected absolute levels but showed moderate repeatability and low correlation with arterial-spin labelling, used as a reference perfusion imaging method.

Another study included in the context of this doctoral thesis dealt with the issue of partial-volume effects in the voxel selected to represent blood. By rescaling the area under the curve (AUC) of the concentration-versus-time curve measured in an artery (assumed to show the desired shape), with the AUC of a large vein, measured under circumstances more favourable for blood-data registration, CBF and CBV values were calibrated. This method aims primarily to correct for partial volume effects in the blood voxel (i.e. it does not directly address relaxivity issues). An observation of interest in this context was that absolute perfusion levels similar to what was expected from literature data were obtained. Furthermore, the repeatability was more promising using this approach, compared to the ones described above.

The MRI signal is represented by a complex number and can be described as a vector in the complex plane, and the most common imaging method in MRI is to study the length or magnitude of this vector. However, the phase of the MRI signal is related to the magnetic field strength, which, in turn, is related to the magnetic susceptibility. As the contrast agent alters the magnetic susceptibility, it should, in principle, be possible to obtain information about contrast-agent concentration using MRI phase information. This approach was used in three of the studies described in this thesis, for calculation of perfusion-related parameters in relative and absolute terms. These studies indicated that information about (or related to) magnetic susceptibility is a promising method for estimating contrast agent concentration and is thus useful for perfusion measurements, whereas a number of methodological issues still need to be resolved or further investigated. It was also shown that the shape of an arterial $\Delta R2^*$ curve, based on DSC–MRI data, displayed a shape similar to the corresponding curve obtained by using magnetic susceptibility information for assessment of concentration. Thus, the shape of a typical arterial blood concentration curve used in a standard DSC–MRI experiment can probably be regarded reasonably reliable. However, the AUC is likely to be underestimated because of partial-volume effects.

Populärvetenskaplig sammanfattning

Perfusion eller genomblödning är termer som används för att beskriva blodflödet i kroppens allra minsta kärl. Information om perfusion kan vara av stor betydelse för att ställa diagnos vid vissa sjukdomar, eftersom blodet transporterar det syre och den näring som behövs för att upprättahålla vävnadens funktion i kroppen. Ett viktigt exempel där information om perfusion kan vara till nytta för att ställa rätt diagnos är stroke, där perfusionsmätningar kan berätta om en behandling kan vara till nytta för patienten eller om behandlingen i huvudsak kommer att innebära en omotiverad risk i form av biverkningar. Andra exempel där perfusionsmätningar kan användas är i samband med cancersjukdomar, då tumörens aggressivitet kan bedömas med hjälp av perfusionsrelaterad information. Det finns också hopp om att kunskap om blodflödet i tumören, i kombination med annan bildinformation, kan ge information om behandlingseffektivitet redan i ett tidigt skede.

Den här doktorsavhandlingen beskriver hur man kan ta fram bilder över hjärnan som i varje bildelement (pixel) visar hur högt blodflödet är i hjärnvävnaden. Det finns flera bildgivande tekniker som kan generera sådana bilder, men i vårt fall har magnetkameraundersökningar utnyttjats. Fördelen med denna modalitet är att patienten slipper utsättas för joniserande strålning, och detta är en fördel framför allt vid undersökning av barn samt för vuxna som förväntas genomgå många undersökningar. De studier som den här avhandlingen beskriver har fokuserat på en metod som kallas *dynamic susceptiblity contrast magnetic resonance imaging (DSC-MRI)*. Den här metoden är robust och ger bilder av visuellt god kvalitet, men de värden på blodflödet som visas i bilden är ofta högre än de sanna värdena. Detta kan bero på flera olika svårigheter i samband med mätning och beräkning, men ett av de viktigaste problemen är att det är svårt att mäta koncentrationen av kontrastmedel inuti kroppen med hjälp av magnetkamera.

Syftet med det här avhandlingsarbetet har varit att studera och utveckla metoder som gör det möjligt att förbättra bestämningen av kontrastmedelskoncentration samt att korrigera för de fel som uppstår då koncentrationen har felbedömts. Det har visat sig vara möjligt att få fram perfusionsvärden som förefaller trovärdiga om man jämför med resultat från andra bildgivande metoder. I flera av studierna har precisionen i resultaten bedömts genom att man upprepat experimentet på samma person och noterat skillnaden i mätresultat mellan två likvärdiga mätningar. Detta är en viktig aspekt för att bedöma om metoden kan användas kliniskt för patienter. Vissa av metoderna har uppvisat liknande resultat vid de båda mätningarna medan andra har resulterat i en större variation mellan de två mättillfällena.

Ett intressant sätt att bedöma koncentrationen av kontrastmedel är att studera hur kontrastmedlet påverkar den magnetiska susceptibiliteten. Denna storhet utgör

ett mått på graden av magnetisering av ett objekt då det placeras i ett yttre magnetfält. Vävnad har generellt sett låg susceptibilitet och påverkas alltså inte i så stor utsträckning av magnetfältet i magnetkameran medan kontrastmedlet påverkas mer. Att mäta den magnetiska susceptibiliteten för att kvantifiera koncentrationen av kontrastmedlet i vävnaden är en relativt ny metod som har utvecklats och utvärderats i de aktuella avhandlingsprojekten. Metoden verkar lovande i det avseendet att den gett rimliga koncentrationsnivåer i vävnaden, vilket i sin tur har medfört att våra uppskattningar av blodvolymen har varit i linje med vad man kan förvänta sig. Avhandlingsarbetena pekar dock också på att den metod som används för att bestämma den magnetiska susceptibiliteten behöver utvecklas för att metoden ska bli robust och pålitlig.

List of original papers

I. **Lindgren E***, Wirestam R, Markenroth Bloch K, Ahlgren A, van Osch MJ, van Westen D, Surova Y, Ståhlberg F, Knutsson L. Absolute quantification of perfusion by dynamic susceptibility contrast MRI using Bookend and VASO steady-state CBV calibration: a comparison with pseudo-continuous ASL. *Magn Reson Mater Phy 2014;27(6): 487-499*

II. Knutsson L, **Lindgren E***, Ahlgren A, van Osch MJ, Bloch KM, Surova Y, Ståhlberg F, van Westen D, Wirestam R. Dynamic susceptibility contrast MRI with a prebolus contrast agent administration design for improved absolute quantification of perfusion. *Magn Reson Med 2014;72(4):996-1006*

III. Wirestam R, **Lindgren E***, van Westen D, Bloch KM, Ståhlberg F, Knutsson L. Cerebral perfusion information obtained by dynamic contrast-enhanced phase-shift magnetic resonance imaging: comparison with model-free arterial spin labelling. *Clin Physiol Funct Imaging 2010;30(5):375-379*

IV. **Lind E**, Knutsson L, Kämpe R, Ståhlberg F, Wirestam R. Assessment of MRI contrast agent concentration by quantitative susceptibility mapping (QSM): application to estimation of cerebral blood volume during steady state. *Magn Reson Mater Phy 2017;30(6):555-566*

V. **Lind E**, Knutsson L, Ståhlberg F, Wirestam R, Dynamic contrast-enhanced QSM for perfusion imaging: A systematic comparison of $\Delta R2^*$- and QSM-based contrast agent concentration time curves. *Manuscript*

* Lind, née Lindgren

List of contributions

The following are my contributions to the original papers included in this thesis:

I. I contributed significantly to the planning and preparation of the study and was responsible for parts of the data collection. I performed most of the post-processing and analysis of the data and made significant contributions to the interpretation of the results. I was the main author of the paper.

II. I participated in the data collection process and extracted some numerical data from images, used for further analysis. I contributed to the writing of the paper by reviewing and commenting on the manuscript.

III. I took significant part in conceptualising ideas. I processed images for further analysis and contributed numerous discussions to the interpretation of the results. I reviewed and commented on all versions of the manuscript.

IV. I had the primary responsibility for project design and was responsible for parts of data collection. I did most of the post-processing and analysis of the data and made major contributions to the interpretation of the results. I was the main author of the paper.

V. I conceived the idea and was responsible for parts of the data collection. I carried out all post-processing of the data and analysis of the results. I made major contributions to the interpretation of the results and was the main author of the manuscript.

Data collection disclaimer regarding Papers I, II, IV and V:

Administration of gadolinium contrast agent (CA) in healthy volunteers on two different occasions is associated with ethical restrictions, and it would seem desirable to maximise the scientific output from such an injection scheme to avoid

the need for additional CA injections, at a later point in time, in the same or another group of healthy volunteers. Hence, the data collection protocol in connection with the contrast agent injection of relevance to Papers I, II, IV and V was designed to accommodate several independent scientific investigations with different hypotheses, to be published separately, and such a multi-study design was also a prerequisite for obtaining approval by the local ethics committee. Parts of the acquired image data have been used for different purposes with clearly separated scientific hypotheses, using independent post-processing approaches and analyses. The resulting publications include appropriate references to other investigations related to the same test-retest CA injection scheme.

Abbreviations

AIF	Arterial input function
ASL	Arterial spin labelling
AUC	Area under curve
BBB	Blood-brain-barrier
CA	Contrast agent
CASL	Continuous ASL
CBF	Cerebral blood flow
CBV	Cerebral blood volume
CF	Correction factor
COSMOS	Calculation of susceptibility through multiple orientation sampling
$CMRO_2$	Cerebral metabolic rate of oxygen
CNR	Contrast-to-noise ratio
CSF	Cerebrospinal fluid
CT	Computed tomography
DCE–MRI	Dynamic contrast enhanced MRI
DSC–MRI	Dynamic susceptibility contrast MRI
EES	Extravascular extracellular space
EPI	Echo-planar imaging
GM	Grey matter
GRE	Gradient echo
Hct	Haematocrit
HEIDI	Homogeneity-enabled incremental dipole inversion
LBV	Laplacian boundary value
MCA	Middle cerebral artery
MEDI	Morphology-enabled dipole inversion
MRI	Magnetic resonance imaging
MTT	Mean transit time
PASL	Pulsed ASL
pCASL	Pseudo-continuous ASL
PDF	Projection onto dipole field
PET	Positron emission tomography
PVE	Partial volume effect
QSM	Quantitative susceptibility mapping
ROI	Region of interest

SAR	Specific absorption rate
SE	Spin echo
SHARP	Sophisticated harmonic artefact reduction for phase data
SNR	Signal-to-noise ratio
SPECT	Single photon emission computed tomography
SVD	Singular value decomposition
SWI	Susceptibility weighted imaging
TE	Echo time
TKD	Thresholded k-space division
tPA	Plasminogen activator
RF	Radio-frequency
US	Ultrasound
VOF	Venous output function
VS-ASL	Velocity-selective ASL
VASO	Vascular space occupancy
WCF	Water correction factor
WM	White matter
XeCT	Xenon-enhanced CT
3D	3-dimensional

1. Introduction

Oxygen and nutrients, required to maintain tissue viability, are transported to tissues of interest by the blood stream. The delivery of these vital substances occurs at the capillary–tissue interface. The volume-flow rate of blood in the capillaries, which are the smallest vessels in the body, is referred to as perfusion. However, a comprehensive description of the blood supply also includes the tissue blood volume and the mean transit time (MTT) (i.e. the average time for blood to travel through the local capillary network) from the arterial to the venous side. Additionally, information about the leakiness or permeability of capillaries is sometimes warranted. The focus of studies reported in this thesis was to quantify perfusion and other perfusion-related parameters (blood volume and MTT) of the brain.

The goal of perfusion imaging is to obtain a digital image in which each pixel represents the numerical value of perfusion or another perfusion-related parameter. Several medical imaging techniques, including single photon emission computed tomography (SPECT), positron emission tomography (PET), computed tomography (CT), ultrasound (US), and magnetic resonance imaging (MRI), can provide useful perfusion maps. One advantage of using MRI is that is does not expose the patient to ionising radiation. This is important, especially for younger patients and those expected to experience many examinations to follow the progress of a disease or to monitor the effects of treatment. Another important argument favouring MRI is that a number of various image contrast patterns can be obtained to emphasise different tissue characteristics of the region of interest (ROI), and the perfusion measurement can thus be combined with MRI methods showing other types of image contrast during the same imaging session to get a complete understanding of relevant tissue properties.

Using MRI, there are mainly three different techniques that provide information about perfusion and/or transcapillary permeability. In two of these techniques, an exogenous contrast agent (CA) is used to monitor the passage of blood in the tissue of interest. These two techniques are referred to as dynamic susceptibility contrast MRI (DSC–MRI) and dynamic contrast enhanced MRI (DCE–MRI). There is a third technique, called arterial spin labelling (ASL), which is based on the use of a radio-frequency (RF) pulse for labelling of endogenous water, using spin inversion in a tissue-supplying artery to enable perfusion quantification by measuring the subsequent effect of labelled spins on the signal in the tissue of

interest. DSC–MRI provides information about three central parameters, i.e. cerebral blood flow (CBF), cerebral blood volume (CBV), and MTT. However, owing to methodological difficulties, further described below, standard implementations of DSC–MRI are only expected to provide relative values of CBF and CBV. Using standard procedures for DSC–MRI measurements, the resulting values of CBF and CBV are often highly overestimated, compared with gold-standard perfusion imaging techniques [1].

In several applications, it is desirable to know the true perfusion level in absolute terms. For example, if accurate perfusion estimates were easily available, a perfusion-based tissue viability threshold approach in stroke patients might facilitate decisions of whether or not treatment with thrombolytic drugs should be employed [2-4]. Absolute perfusion values are also beneficial in longitudinal studies, where the perfusion is monitored over time, and to enable comparisons among different individuals or between different MRI sites.

To calculate CBF, CBV, and MTT by DSC–MRI, a time series displaying how the concentration of CA varies during its passage is required for each voxel, and the main reasons for the commonly overestimated DSC–MRI CBV and CBF values are associated with incorrect CA concentration estimates. These problems originate, for example, from the intricate and non-linear relationship between MRI signal and CA concentration and from partial volume effects (PVEs), which tend to complicate the concentration estimation in blood. In this doctoral thesis, different strategies to register the effect of the CA and to estimate its concentration are reported. Some of the methods are used to provide an alternative measure of blood volume, which can be used to calibrate perfusion information from DSC–MRI, whereas others are used to correct for PVEs in the artery used for CA concentrations in the blood. A comparison of how the standard DSC–MRI methodology performs, compared to a new CA quantification approach, is also included.

1.1. Aims

The general aims of the studies reported in this thesis are to improve and validate calibration approaches for perfusion estimates obtained by DSC–MRI and to improve quantification of CA concentration in vivo. The specific aims for each paper are summarised below:

- *Paper I*: To calibrate perfusion estimates from DSC–MRI by an independent blood volume measurement and validate the results against a reference perfusion imaging method.

- *Paper II*: To correct perfusion values from DSC–MRI by employing an additional dynamic CA-enhanced measurement in pure blood using a lower dose of CA.
- *Paper III*: To investigate the potential of using the phase of the MRI signal for relative measures of CA concentration in dynamic perfusion measurements.
- *Paper IV*: To employ quantitative values of the magnetic susceptibility of the CA in the steady-state period (after the first passage) to estimate blood volume.
- *Paper V*: To estimate CA concentration during the contrast-enhanced MRI time series using the change in magnetic susceptibility, with emphasis on voxels typically selected to represent blood in a standard DSC–MRI protocol.

2. Microcirculation

2.1 Physiological background

The capillary diameter is approximately 5–10 μm [5], and the blood velocity in the capillaries is of the order of a few mm/s, compared to the velocity of blood in large arteries, which can be tens of cm/s [6]. Oxygen is carried by the red blood cells, whereas nutrients, such as proteins, glucose, vitamins, amino acids, and lipid [5], are transported by the blood plasma [5]. In addition to red blood cells and plasma, the blood also comprises white blood cells, which are involved in the immune system, and platelets, which are important for ability of the blood to coagulate [5]. The volume fraction of the whole blood occupied by red blood cells is called the haematocrit, and it varies with the diameter of the vessel [7]. In an MRI experiment, the CA is situated in the blood plasma, and it is important to realise that the haematocrit needs to be considered in the quantification of blood volume and flow in methods where the CA concentration is compared between capillaries and large vessels. This is relevant to all papers in this thesis.

As mentioned above, perfusion describes the volume-flow rate of blood in the capillary network per unit mass (or volume) of tissue and is often expressed in units of ml/min/100 g (or ml/min/100 ml). According to a summation of literature values by Donahue et al. [8], the range of CBF values in normal grey matter (GM) of the brain is 35–60 ml/min/100 g [8], and the corresponding range for white matter (WM) is 17–28 ml/min/100 g [8]. However, the values show substantial individual variations, and CBF tends to decrease with age [9]. Furthermore, CBV is the volume fraction of blood per unit mass (or volume) in a tissue sample and is often expressed in units of ml/100 g or ml/100 ml, and MTT is the average time it takes for blood to pass through the capillary system from the arterial to the venous side, in units of seconds. Values of CBV in healthy tissue range between 3.5 and 6.6 ml/100 g in GM [8] and between 2.1 and 3.0 ml/100 g in WM [8]. MTT values in GM and WM are quite similar, with ranges of normal values of 3.8–6.6 in GM [8] and 4.6–7.4 in WM [8].

In principle, the perfusion can be modified by changes in the volume fraction of blood in the tissue sample of interest and/or by changes in the velocity at which the blood flows through the capillaries. It is important for the tissue to regulate CBF and, in particular, to keep it above a certain viability threshold. In some conditions of changed perfusion pressure, CBV and MTT can be altered to ensure

that CBF is maintained [10,11]. Hence, to describe the microcirculation in more detail, with respect to the effects of autoregulation, the additional parameters, CBV and MTT, are required. The relationship between CBF, CBV, and MTT is given by the central volume theorem [12]:

$$CBV = CBF \cdot MTT. \quad (1)$$

As mentioned in the introduction, one particular advantage of DSC–MRI, the perfusion measurement method evaluated and developed in this thesis work, is that all three parameters are obtained.

2.2 Clinical relevance of brain perfusion assessment

One potentially important clinical application of perfusion measurements is in ischemic stroke, where information about perfusion can help in the decision of whether or not to treat the patient with a plasminogen activator (tPA) [13]. It has been proposed that regions showing a mismatch between observed lesion patterns in perfusion and diffusion imaging (i.e. tissue with impaired blood supply but unaltered diffusion) can be used to assess whether some of the tissue is salvageable by treatment [13-15]. Information about MTT can enhance this type of assessment in stroke patients, because MTT is often increased in the compensatory process of maintaining CBF [11]. Owing to the rather low GM-to-WM MTT contrast of healthy tissue, regions with prolonged MTT, associated with the so-called ischaemic penumbra, are often clearly visible in MTT maps [11]. Thus, treatment with tPA, associated with a certain risk for haemorrhage [16], can be avoided in cases where it is unlikely to provide a positive effect. The combined information from perfusion and diffusion imaging is a strong argument for MRI perfusion measurements in stroke patients, compared to other imaging techniques.

CBF and CBV information can also be valuable in identifying and grading intracranial tumours. For example, both CBF and CBV have shown higher values in more aggressive type of gliomas [17]. Some neurodegenerative diseases are also associated with altered perfusion. For example, patients with Alzheimer's and Parkinson's diseases exhibit regions with lower CBF values [18]. Perfusion can also be increased in patients with migraines [3], and perfusion imaging can be valuable for diagnosis of diseases, such as carotid occlusion and Moyamoya disease [13].

2.3 Quantitative perfusion levels

The focus of the studies presented in this thesis is improving quantification of CBF and CBV estimates in absolute terms, because several previous studies have indicated that obtained values tended to be significantly overestimated when standard DSC–MRI methodology is employed [19-21]. In some applications, it is sufficient to visually inspect focal lesions in a perfusion image or to compare relative values of perfusion among different tissues. However, in other cases, it is of value to know the absolute perfusion levels, such as with ischemic stroke, tumour grading, and depression. With strokes, a perfusion threshold has been discussed as a means to decide whether or not to treat the patient [2-4], whereas for tumours, knowledge of the perfusion level can improve the accuracy of tumour grading [22,23]. For patients with depression, studies suggest that a global change in perfusion is expected, and this cannot be recognised if only relative perfusion values are available [24,25].

Absolute levels are warranted when comparing results from examinations performed at different points in time, for example, during a prolonged treatment period and for comparisons between different patients and different MRI sites.

3. Theory of perfusion measurement

3.1 Basic tracer-kinetic considerations

The theory used for calculations of CBF, CBV, and MTT in DSC–MRI is based on theory presented by Meier and Zierler [12,26,27], relying on Fick's principle of mass conservation. This theoretical framework has been reviewed and reformulated by others [28-30], and the main relationships used in DSC–MRI are derived below, based on a combination of the above-mentioned references. The theory can be applied to any system meeting the requirements. However, in the context of this thesis, notations applying to the flow of blood in vessels are adapted. In Fig. 1, a system sketch is presented, showing one inflow vessel and one outflow vessel, coupled with a network of many small vessels with different pathways. The blood flows from A to B with flow F expressed as volume per unit time (i.e. formally the volume flow rate), and a tracer that is transported by the blood is assumed to be injected at A. For the model to be valid, certain conditions must be fulfilled. The flow should be constant, and the possible pathways through the system should remain unchanged during the time of measurement. Additionally, the injected tracer must follow the same kinetics as the blood, and all tracer particles must leave the system through B (i.e. no particles can stay in the volume of distribution V_D). Depending on the tracer, the volume, V_D, can be interpreted in different ways. In cerebral applications with an intact blood-brain-barrier (BBB), as assumed in DSC–MRI, the gadolinium tracer does not leave the blood and the volume V_D corresponds to the intravascular space.

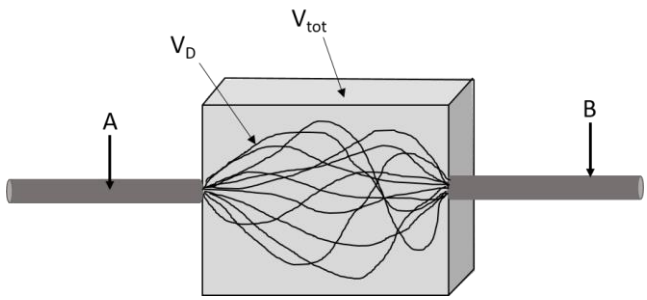

Figure 1. Schematic of the vascular system used to derive expressions used for estimation of perfusion parameters.

3.1.1 Simplified system

For the simple system shown in Fig. 1, it is assumed that an amount, Q, of tracer particles (moles) is injected at A as an ideal bolus (i.e. a Dirac delta function). All tracer particles arrive at the inlet of volume V_D at the same time, but may take different pathways to B and will thus not arrive at B at the same time. Thus, there will be a distribution of transit times, and this distribution is described by the function, h(t), which gives the probability of a particle, having been injected at A at time t = 0, to arrive at B at time t. As one of the assumptions mentioned above, all tracer particles must leave volume V_D through B. One property of h(t) is that

$$\int_0^\infty h(t)dt = 1. \tag{2}$$

The cumulative distribution function, H(t), can thus be described as the fraction of tracer particles reaching B during the interval of time 0 to time t.

$$H(t) = \int_0^t h(\tau)d\tau. \tag{3}$$

Furthermore, the residue function, R(t), expresses the fraction of all injected tracers remaining in the volume, V_D, at time t.

$$R(t) = 1 - \int_0^t h(\tau)d\tau = 1 - H(t). \tag{4}$$

For a simple system as described here, flow, F, can, in principle, be estimated by measuring the concentration over time at the outlet and the total amount of tracer particles, according to Eq. 5.

$$F = \frac{Q}{\int_0^\infty C_B(t)dt}. \tag{5}$$

Here, $C_B(t)$ represents the concentration of tracer particles at point B at time t. Additionally, as stated in the second mean value theorem, MTT can easily be determined from h(t) as

$$MTT = \int_0^\infty th(t)dt. \tag{6}$$

Furthermore, volume V_D can be found by integrating all possible transit times:

$$V_D = F\int_0^\infty th(t)dt. \tag{7}$$

Here, a derivation of the central volume theorem (mentioned earlier) is demonstrated as the relationship, $V_D = F \cdot MTT$ [12]. This can easily be obtained by combining Eqs. 6 and 7.

3.1.2 Modifications of the model in a realistic system

For in vivo measurements, it is not feasible to inject the tracer during an infinitely short time in a direct connection with the inlet to capillary system. Thus, the tracer will not enter as an ideal bolus. Additionally, measurements at point B are not easy to implement, and the relevant relationships should be adapted to a more realistic measurement situation. The amount of tracer particles having passed point A at time t, $Q_A(t)$, can be described according to

$$Q_A(t) = F \int_0^t C_A(\tau) d\tau, \tag{8}$$

where $C_A(\tau)$ is the concentration of tracer particles at A, measured at each point in time. For the simplified system, the amount having passed through B can easily be described as Q_A times the cumulative distribution function, H(t), because the only thing differentiating the individual tracer particles is the specific pathway, because they all enter the volume, V_D, at the same time. For a more realistic system, the tracer particles enter volume V_D at different times according to a temporally distributed input function. For example, with DSC–MRI, a tracer is injected into an arm vein, and the compact volume of the tracer (i.e. the bolus) will thus be distributed in time because of the finite injection time but also during the passage through the main circulatory system before it enters the tissue of interest. Hence, the concentration of particles measured at B at time t depends on both the input function at point A (i.e. the particles enter at different times, τ) and on H(t), as described by Eq. 9:

$$C_B(t) = \int_0^t C_A(t) h(t-\tau) d\tau. \tag{9}$$

Note that, in Eq. 9, a division by the tissue volume has been incorporated to obtain concentration C instead of the amount of particles, Q. The amount of tracer particles having passed B can be expressed as follows, similarly to Eq. 8:

$$Q_B(t) = F \int_0^t C_B(\tau) d\tau. \tag{10}$$

As mentioned above, it is difficult to perform measurements at B. Thus, it is common to study the amount of particles in a total tissue volume, V_{tot}, that instead includes V_D. The amount of particles in V_{tot} can be expressed as the difference between the amount of particles having passed A and B at a given time. Note that the amount of particles in V_{tot} is the same as the amount of particles in V_D. By combining Eqs. 8–10 and using the relationship between h(t) and R(t) from Eq. 4, it can be seen that

$$Q_V(t) = Q_A(t) - Q_B(t) = \tag{11}$$

$$= F\int_0^t C_A(\tau)d\tau - F\int_0^t \left(\int_0^t C_A(t)h(t-\tau)d\tau\right)dt =$$

$$= F\int_0^t C_A(t)\cdot R(t-\tau)d\tau.$$

Finally, division of Q_V by the total tissue volume, V_{tot}, is performed to obtain the tissue concentration, C_{Vtot}. Additional multiplication of the right-hand side by the density of tissue, ρ, yields the perfusion, $f = Q_V/(V_{tot}\rho)$, in units of ml/min/100 g.

$$\mathrm{C_{Vtot}}(\mathrm{t}) = f\rho\int_0^t C_A(t)\cdot R(t-\tau)d\tau. \tag{12}$$

Equation 12 is a convolution integral, and the notation, ⊗, for convolution is commonly used:

$$\mathrm{C_{Vtot}}(\mathrm{t}) = f\rho[C_A(t)\otimes R(t)]. \tag{13}$$

Hence, if $C_{Vtot}(t)$ and $C_A(t)$ are measured, a deconvolution of $C_{Vtot}(t)$ with $C_A(t)$ yields the residue function scaled by the perfusion and the density of the tissue (i.e. $R_{Sc}(t) = f\rho R(t)$), and $R_{Sc}(t)$ is sometimes referred to as the tissue impulse response function. By definition, R(0)=1, because R(0) represents the fraction of the injected amount of tracer that remains in the volume, V_D, after an ideal bolus injection. Hence, the perfusion can be determined directly as the $R_{Sc}(0)$ value.

The amount of tracer, situated in the volume, can be expressed in terms of concentration and volume: either the distribution volume V_D or the total volume V_{tot}.

$$\mathrm{Q_V}(t) = C_{Vtot}(t)\cdot V_{tot} = C_{VD}(t)\cdot V_D. \tag{14}$$

Because Eqs. 8 and 10 are valid, and the mass must be conserved, it can be concluded that [28]:

$$Q = F\int_0^\infty C_A(t)dt = F\int_0^\infty C_B(t)dt = F\int_0^\infty C_{VD}(t)dt. \tag{15}$$

The blood volume, V, is the fraction of the volume of interest that comprises blood, and the expression usually employed to estimate blood volume can be found by combining Eqs. 14 and 15. The density is included to get the familiar unit of ml/100 g.

$$V = \frac{V_D}{\rho V_{tot}} = \frac{C_{Vtot}(t)}{\rho C_{VD}(t)} = \frac{\int_0^\infty C_{Vtot}(t)\,dt}{\rho \int_0^\infty C_{VD}\,(t)dt} = \frac{\int_0^\infty C_{Vtot}(t)dt}{\rho \int_0^\infty C_A\,(t)dt}. \quad (16)$$

The expression for MTT, as stated in Eq. 6 $\left(MTT = \int_0^\infty th(t)dt\right)$, is still valid for the realistic system. The transit time distribution function, h(t), is, however, normally not available. Instead, the relationship between h(t) and the residue function, as stated in Eq. 4 $\left(R(t) = 1 - \int_0^t h(\tau)d\tau\right)$, is utilised to find a convenient expression for MTT. Following Eq. 4, the derivative of R(t) is

$$\frac{dR(t)}{dt} = -h(t). \quad (17)$$

By performing an integration by parts of $1 \cdot R(t)$ [29], the following expression is obtained:

$$\int_0^\infty R(t)dt = \lim_{t\to\infty}[tR(t)] + \int_0^\infty th(t)dt. \quad (18)$$

Because $tR(t) \to 0$ when $t \to \infty$ [12], MTT can be calculated as the integral of the residue function, R(t):

$$MTT = \frac{\int_0^\infty R_{Sc}(t)dt}{R_{Sc}(0)} = \int_0^\infty R(t)dt. \quad (19)$$

The middle part of Eq. 19 is sometimes referred to as Zierler's area-to-height relationship. A combination of Eq. 16 and the central volume theorem ($V = f \cdot MTT$) yields an alternative expression for f:

$$f = \frac{V}{MTT} = \frac{\frac{\int_0^\infty C_{Vtot}(t)dt}{\rho \int_0^\infty C_A(t)dt}}{\frac{\int_0^\infty R_{Sc}(t)dt}{R_{Sc}(0)}} = \frac{R_{Sc}(0) \cdot \int_0^\infty C_{Vtot}(t)dt}{\rho \int_0^\infty C_A(t)dt \cdot \int_0^\infty R_{Sc}(t)dt}. \quad (20)$$

As discussed further in Chapter 5, Eqs. 16, 19, 13, and 20 are frequently used for estimating CBV, MTT, and CBF.

Table 1. Quantities involved in tracer kinetics including typical units

PARAMETER	DESCRIPTION
$C_A(t)$	Concentration of tracer particles at A (in M)
$C_B(t)$	Concentration of tracer particles at B (in M)
C_{VD}	Concentration of tracer particles (in M) in the distribution volume V_D
C_{Vtot}	Concentration of tracer particles (in M) in the total volume V_{tot}
F	Volume flow rate (in ml/min)
f	Perfusion (in ml/min/100 g)
H(t)	Cumulative distribution function
h(t)	Transit time distribution function
MTT	Mean transit time (in s)
Q	Total amount of tracer (in moles) injected to the system
Q_A	Amount of tracer (in moles) that has passed A
Q_B	Amount of tracer (in moles) that has passed B
Q_V	Amount of tracer (in moles) residing in V_{tot} or V_D.
$R_{Sc}(t)$	Impulse response function resulting from deconvolution, $R_{Sc}(t)=f\rho R(t)$
R(t)	Tissue residue function
V	Blood volume (in ml/100 g)
V_D	Distribution volume (in ml). Corresponds to the intravascular space in DSC–MRI
V_{tot}	Total tissue volume of interest (in ml). Corresponds to intravascular+extravascular space in DSC–MRI
ρ	Density (in g/ml)

4. Overview of different techniques for perfusion imaging

The projects reported in this doctoral thesis focused primarily on development and validation of perfusion measurements based on DSC–MRI data, and this technique is described in detail in the next chapter. Several other methods providing perfusion maps exist, using MRI and other imaging modalities. Thus, a brief description of other methods is given below, followed by a somewhat more detailed discussion about MRI-based methods.

4.1 Nuclear medicine

In nuclear medicine, ionizing radiation from an internally distributed radioactive tracer is used for medical imaging. In PET, a positron-emitting radionuclide is employed, and the two resulting annihilation photons are detected outside the body for reconstruction of a 3-dimensional (3D) volume. In SPECT, a photon-emitting radionuclide is used. For perfusion measurements, the tracer can either be inhaled or injected into a vein [31]. Several techniques, based on different radioactive tracers, exist for perfusion measurements, with the most common radionuclide being ^{15}O for CBF PET [32] and ^{99m}Tc, ^{123}I, and ^{133}Xe for CBF SPECT [31,32], all coupled to different types of molecules with specific properties in the body. Perfusion values from PET measurements are often regarded as the gold standard method for quantification in absolute terms. Most of the SPECT perfusion measurements show relative perfusion estimates. However, it is also possible to achieve absolute quantification using ^{133}Xe SPECT [31,32].

4.2 Computed tomography

Perfusion measurements are also feasible with techniques involving CT, using either xenon or iodine as a CA. In Xenon-enhanced CT (XeCT), a stable isotope of xenon is inhaled to eventually diffuse through the BBB [32]. The use of iodine CA

is based on intravenous injection, followed by dynamic imaging during the first passage in the vascular system [32], similar to DSC–MRI. This method provides CBV, CBF, and MTT. Both methods are capable of delivering quantitative perfusion values in absolute terms [32]. However, dynamic CT share some (albeit not all) of the difficulties associated with DSC–MRI. For CT, it is fairly straightforward to determine the concentration of CA, because the change in attenuation caused by the CA is proportional to the concentration. This facilitates quantification [33].

4.3 Ultrasound

In US, microbubbles can be used as a tracer, because they alter the frequency and phase of the signal. Perfusion can be estimated by injecting microbubbles and monitoring their intravascular passage through the vascular system [34]. Unlike many other tracers, it is possible to remove the tracer while in the system, because the microbubbles can be destroyed by high-intensity US. Thus, as an alternative method, after elimination of all microbubbles in the imaging volume, it is possible to follow the renewed accumulation of tracer and to estimate perfusion by studying the initial slope and the plateau of the accumulation curve [34].

4.4 Dynamic contrast-enhanced MRI

An alternative or complementary method to DSC–MRI is DCE–MRI, primarily used to obtain information about plasma volume and transcapillary permeability. DCE–MRI is applicable not only to the brain, but also to many other organs of the body, because the theory behind DCE–MRI does not assume that the CA remains in the vascular space [29]. With DCE–MRI, T1-weighted images are collected for a period of several minutes (typically of the order of 5 min) before, during, and after intravenous injection of CA [35]. A T1 map is also obtained before the injection of CA, and a pharmacokinetic model is then fitted to the experimental signal data. With DCE–MRI, different models exist, depending on the specific application and on the quality of data. However, the most commonly used approach is the so-called extended Tofts model, which requires concentration-versus-time curves in both tissue and blood [35]. It should be noted that, in DCE–MRI, the parameters resulting from the calculations are not always a direct measure of perfusion. Instead, the composite parameter, K^{trans}, is often estimated, showing different physiological meanings, depending on the physiological circumstances. For situations where the perfusion is sufficiently high, compared to capillary permeability, K^{trans} describes the permeability-surface area product,

which is the combination of the permeability of the vessel and the surface area of the vessel per unit mass of tissue. This describes the extent to which the CA leaks from the vascular system. However, for systems with limited perfusion in relation to permeability, the amount of CA leaking from the vascular system to the surrounding tissue is not predominantly dependent on the permeability of the vessel but instead of the availability of CA (i.e. on the inflow). Thus, for systems with limited perfusion, the parameter, K^{trans}, reflects perfusion [29,35].

4.5 Arterial spin labelling

Another MRI-based method for perfusion imaging is ASL, which is a completely non-invasive method in the sense that no exogenous CA needs to be injected. Hence, in contrast to other MRI-based methods, it is easy and unproblematic to perform repeated measurements during a short period. Additionally, for some patients suffering from impaired renal function, injection of gadolinium (Gd) CA may constitute a risk of developing nephrogenic systemic fibrosis [36]. In ASL, RF pulses are used to invert (or saturate) the spin magnetisation of arterial blood, upstream to the tissue of interest. The saturated/inverted spin magnetisation serves as an endogenous tracer transported to the tissue of interest. The basic idea in ASL is to collect two different types of images, one where the blood water spins are labelled (or tagged), and one without any labelling, referred to as the control image. When the labelled blood has entered the imaging volume, a reduced MRI signal can subsequently be measured, owing to the fact that the magnetisation of the inverted spin population subtracts from the original longitudinal magnetisation of the static spins in the tissue. The MRI signal difference between the labelled image and the control image, denoted ΔM, is proportional to the perfusion,

$$\Delta M = M_{control} - M_{tagged} \propto CBF. \tag{21}$$

The signal difference, ΔM, depends on the labelling approach, but is generally not more than a few percent of the control-image signal [37,38]. Thus, to increase the signal-to-noise ratio (SNR) in the resulting perfusion maps, the labelled and control image acquisitions are normally repeated several times during an ASL experiment. In ASL, the tracer is labelled water, which is almost freely diffusible. Thus, it is possible for the tracer to leave the vascular system during the experiment [39]. Additionally, the inverted blood magnetisation will experience T1 relaxation as soon as the labelling is completed, and the tracer will thus gradually be reduced during the measurement [37,39].

4.5.1 Different ASL labelling approaches

In ASL, several different techniques for labelling arterial blood exist. In continuous ASL (CASL), blood is labelled in a thin slice, close to the imaging volume, using a long label duration of about 2–4 s [38-40]. Because the labelling slice is positioned close to the imaging volume, less T1 relaxation of the labelled blood spins occurs before entering the imaging volume, and CASL thus provides perfusion maps with high SNR [37]. However, a standard clinical MRI scanner is normally not capable of emitting RF energy during a sufficiently long period, and special equipment is therefore necessary. The long labelling duration is also associated with high specific absorption rate (SAR) [40].

A similar method, without the need for special equipment, is pseudo-continuous ASL (pCASL) in which a long labelling period is achieved via many repeated short RF pulses. As in CASL, a thin labelling slice close to the imaging volume is used. With this technique, a reasonably high SNR [37] is obtained without the high SAR levels associated with CASL[39].

Another category of labelling technique is referred to as pulsed ASL (PASL), where blood spins in a large labelling slab of 10–15 cm are labelled during a short duration of 5–20 ms [39]. With this technique, SAR is low at the expense of low SNR, because fewer blood spins are inverted, compared to other techniques, and because the inverted spins must travel some distance between the labelling location and the imaging volume. They will thus experience T1 relaxation during that time [37,38].

Another ASL approach is called velocity-selective ASL (VS-ASL). With this method, the labelling volume also includes the imaging volume, but only blood moving with a velocity above a certain threshold value (e.g. 1 cm/s) is labelled [38]. The major advantage of VS-ASL is that it is not sensitive to artefacts related to different transit delays, which reflects the time it takes for the labelled blood to reach the imaging volume [38,39].

In the ASL method called quantitative STAR labelling of arterial regions (QUASAR) [41], quantification is based on the convolution integral described in Eq. 12. By measuring ΔM at different inversion times (i.e. the time between the labelling and the imaging of the volume of interest) a curve showing the perfusion-weighted ΔM signal as a function of time is obtained. Hence, once an AIF can be estimated from the experiment, perfusion f can be calculated by solving the convolution integral (Eq. 12), as further specified in Section 4.5.2.

In 2015, a consensus paper from the perfusion study group of the *International Society for Magnetic Resonance in Medicine (ISMRM)* and the *European Consortium for ASL in Dementia* was published, in which pCASL was recommended as the preferred method for clinical use [37]. In the study reported in Paper I, pCASL was used as a reference method for comparison with the CA-based perfusion methods under evaluation. The pCASL data obtained in the

Paper I study showed good repeatability, demonstrated by high correlation between measurements in the same volunteer on two different occasions. However, the drawback of using pCASL in Paper I was that the labelling failed in some of the volunteers, leading to perfusion images in which some regions of the brain showed very low apparent CBF.

4.5.2 Quantification of perfusion using ASL

As described above, the MRI signal difference between the labelled and the control image is proportional to the perfusion. However, with certain assumptions and information about the imaging parameters, it is possible to obtain absolute levels of perfusion with ASL. The methods for quantification differ between different labelling techniques [37]. In the quantification method used in the study reported in Paper I, where the pCASL sequence was used, the signal difference can be described as [42,43]:

$$\Delta M = 2 \cdot M0_a \cdot \alpha \cdot CBF \cdot T1_a \cdot \left(1 - e^{-\frac{\tau}{T1_a}}\right) e^{-\frac{\omega}{T1_a}}, \quad (22)$$

where $M0_a$ is the signal intensity of blood at equilibrium, α is the label efficiency, $T1_a$ is the longitudinal relaxation time in arterial blood, τ is the label duration and ω is the time between labelling and imaging of the volume of interest.

All parameters in Eq. 22 are either MRI scanner settings or data that can be found in the literature, except for $M0_a$, which must be measured for each examination. Because $M0_a$ corresponds to the signal in blood at $TR \rightarrow \infty$, it cannot be directly measured in the labelled or control images. Instead, an additional scan with identical parameters, except for a very long TR, can be utilised to find the signal in blood [37]. However, in practice, owing to PVEs, it is not always easy to find the signal in a voxel containing only arterial blood. Thus, as described in Paper I, the signal in arterial blood at $TR \rightarrow \infty$ can be calculated from a measurement in WM at very long TR, according to:

$$\mathrm{M0_a} = \frac{S_{WM}}{\left(1 - e^{-\frac{TR_{ref}}{T1_{WM}}}\right) \cdot \left(e^{-\frac{TE_{ref}}{T2^*_{WM}}}\right)} \cdot \frac{\lambda_a}{\lambda_{WM}} \cdot e^{-\frac{TE}{T2^*_a}} \cdot \rho. \quad (23)$$

Here, S_{WM} is the signal intensity in WM, λ_a and λ_{WM} are the fractions of water in arterial blood and WM, respectively, and ρ refers to the density of brain tissue to obtain CBF in ml/min/100 g.

In the study described in Paper III, QUASAR was used as a reference method, for comparison with phase-based CBF estimates. In QUASAR, ΔM is obtained at different inversion times, and CBF can thus be estimated by deconvolution of ΔM in tissue with the AIF (see Eq. 12). The shape of the AIF is obtained from the

difference between data from sequences without and with bipolar crusher gradients. The crusher gradients cause moving spins to dephase, and this sequence will thus provide images without the intravascular signal. A correct amplitude of the AIF is obtained by considering the label duration and $M0_a$, and by scaling the AIF to the correct arterial blood volume (aBV) fraction for each voxel [41]. With this approach, a reasonable repeatability was found in a multi-centre study, including 28 sites [44].

4.6. Estimation of CBV using measurements of contrast agent concentration in the steady-state period

Following CA injection into an arm vein, an arterial bolus of CA enters the brain, passes the microvasculature of the brain tissue, and leaves the brain on the venous side. After some time, a second passage of CA can be seen, referred to as the recirculation phase. This effect occurs at approximately 30 s after the initial rise of the CA concentration, as can be seen in the concentration curves shown in Fig. 2 and in Paper V. After the second passage (i.e. after the first recirculation), a fairly stable non-zero level of CA is reached. This is referred to as the steady-state period. In the steady state, the concentration of CA decreases slowly and can be assumed constant during the remaining time of measurement. Considering that CA is present in the vasculature also at steady state, properties such as relaxation times and magnetic susceptibility are altered, compared to the baseline. The differences in parameters, depending on CA concentration between baseline and steady state, can be utilised to estimate CBV. Three different strategies used in Papers I and IV, are described below.

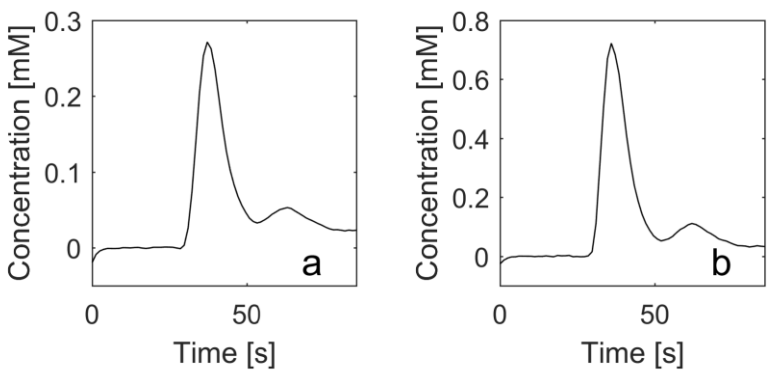

Figure 2. Concentration-versus-time curves in (a) GM and (b) a voxel representing blood from a typical DSC–MRI experiment. Relaxivity values for tissue ($r2^* = 85\ s^{-1}mM^{-1}$) and AIF ($r2^* = 91\ s^{-1}mM^{-1}$) from Papers IV and V were used to convert $\Delta R2^*$ values to concentration.

4.6.1 Change in longitudinal relaxation time, used in the Bookend technique

In the study reported in Paper I, the shortening effect of CA on the longitudinal relaxation time, T1, was used to estimate CBV. By relating the change in tissue relaxation rate (i.e. 1/T1) to the altered relaxation rate in blood, CBV can be estimated according to Eq. 24 [45].

$$CBV^{FastEx} = 100 \cdot \frac{1}{\rho} \cdot \frac{1 - Hct_{LV}}{1 - Hct_{SV}} \cdot \frac{\left(\frac{1}{T1_{post}} - \frac{1}{T1_{pre}}\right)_{tissue}}{\left(\frac{1}{T_{post}} - \frac{1}{T1_{pre}}\right)_{blood}}. \quad (24)$$

Hct_{LV} and Hct_{SV} represent the haematocrit values in large and small vessels, respectively, considering that the CA is situated only in plasma. $T1_{pre}$ and $T1_{post}$ represent the longitudinal relaxation times at baseline and at steady state, respectively, and ρ is the density of brain tissue. Examples of images of $T1_{pre}$, $T1_{post}$, and CBV estimated by the Bookend approach are shown in Fig. 3.

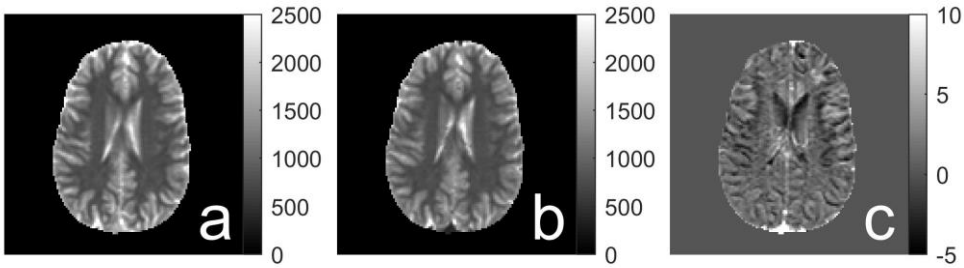

Figure 3. Images showing (a) T1 before CA administration, (b) T1 after CA administration, and (c) CBV. Note that the CBV image is only for visualisation purposes; CBV was calculated from regions of interest in the Paper I study. T1 is shown in ms and CBV in ml/100 g.

As indicated by the notation, CBV^{FastEx}, in Eq. 24, the relationship is valid when the exchange of water molecules between the intravascular space and the extravascular extracellular space (EES) can be regarded as fast. Under such an assumption, the diffusion of water molecules between the intravascular space and the EES is sufficiently rapid to assure that all water molecules in the tissue volume are affected by the CA, whereas the CA is distributed only in the intravascular compartment. Hence, all tissue molecules experience longitudinal relaxation to a degree that is determined by the mean voxel CA concentration, and the model based on the change in tissue longitudinal relaxation rate would be appropriate [45-47]. In the case of slow-water exchange, the difference in MRI signal in a T1-weighted MRI sequence would instead be the appropriate quantification approach

[45-47]. However, whereas it has been shown that the fast-exchange model is most reasonable, neither the fast-exchange nor the slow-exchange model is completely valid for the actual measurement situation in tissue. Thus, a water correction factor (WCF) needs to be implemented to account for the deviation from the fast water-exchange limit. Using literature values of CBV_{true}, the WCF can be estimated by plotting CBV_{true}/CBV^{FastEx} as a function of the CA-induced change in relaxation rate in blood, $\Delta R1_{blood}$, and fitting a curve of the form $a \cdot \Delta R1^2 + b \cdot \Delta R1 + c$ to the data [45,48,21]. Unless the WCF is applied, the assumption of fast water exchange would result in underestimated CBV values, whereas the assumption of slow water exchange would, correspondingly, lead to overestimated CBV values [45,46]. It should be noted that the validity of the fast exchange limit approach depends on the CA concentration levels (taken into account by the WCF), but also on the MRI imaging parameters [46]. Thus, the WCF should be individually estimated for each specific MRI pulse sequence used to measure T1. When the WCF is defined, CBV can be calculated according to

$$CBV = WCF(\Delta R1) \cdot CBV^{FastEx}. \quad (25)$$

In the work described in Paper I, the approach described above was used to obtain a WCF for the specific MRI pulse sequence employed in the study. This WCF returned CBV values close to reference values, but the model fitting to the measured data was not convincing. In Fig. 4, a comparison of the WCFs described in Paper I (for both WM and GM ROI) are compared to the WCF reported by Shin et al. [48], who measured in WM. The shapes of the WCF curves indicate that a similar degree of correction was required when assuming the fast water exchange limit, implying that the measurement conditions in the Paper I study were similar, regarding water-exchange effects [46], to the experiment reported by Shin et al. [48].

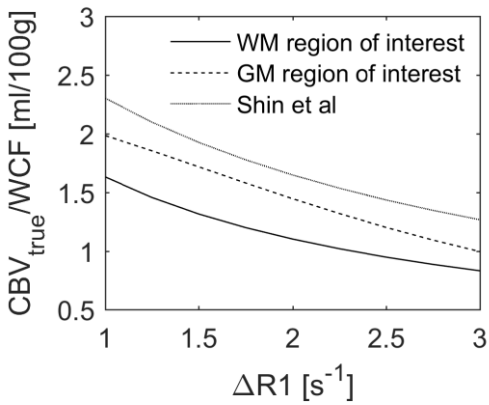

Figure 4. Curves showing the WCF used for CBV estimates with the Bookend method. Curves from Paper I and curve adapted from Shin et al. [48] **are displayed.**

4.6.2 Vascular space occupancy

Another method used to estimate CBV, reported in Paper I, was the vascular space occupancy (VASO) technique. Similar to the Bookend technique, VASO was, in Paper I, also based on the CA-induced shortening of T1 to estimate CBV. In VASO, however, an MRI pulse sequence cancelling the voxel signal components with a T1 of blood (without CA) is used. The difference in MRI signal in a steady state, after the CA injection, and the MRI signal without CA was calculated and compared with the signal from blood to estimate the fraction of blood in the tissue [49].

In an inversion recovery (IR) pulse sequence, the signal difference in a tissue voxel containing both an extravascular and a vascular compartment [49] can be expressed as

$$S_{post} - S_{pre} = \underbrace{S_{extra}^{post} + S_{blood}^{post}}_{S_{post}} - \underbrace{S_{extra}^{pre}}_{S_{pre}} = S_{blood}^{post}. \quad (26)$$

S_{extra} represents the MRI signal from the extravascular part of the tissue voxel, and S_{blood} represents the MRI signal from the intravascular part. 'Pre' and 'post' denote measurements before the CA and in steady state after the injection of CA, respectively. Note that the pre-CA signal lacks the contribution from blood, owing to the blood-nulling IR sequence. Because the CA is assumed to remain in the vascular space, T1 in the extravascular space is unchanged. Thus, the signal from the extravascular part is unaffected by the CA and is cancelled out when the signal difference is calculated. This assumption implies no water exchange between the intra- and extravascular part [49,50]. The validity of this assumption is, however, dependent on the concentration of CA, and the assumption is less valid at high CA concentrations [50]. Because the concentration of CA gradually decreases after the recirculation phase, it is favourable for the experiment to perform the VASO sequence after a period of time. As shown by Uh et al. [50], the best time period is between 7 and 14 min after the CA injection to minimise the effect of water exchange while maintaining high signal difference between the pre-CA and post-CA VASO images.

The signal from blood with CA can be described as [49]

$$S_{blood}^{post} = A \cdot CBV \cdot C_{blood} \cdot \left(1 - 2e^{-\frac{TI}{T1_{blood}}}\right). \quad (27)$$

Factor A describes the MRI signal from water protons at equilibrium (per unit volume). C_{blood} is the water proton density in the intravascular space (ml water per ml blood), and TI is the inversion time. Thus, combining Eqs. 26–27, and

assuming a sufficiently short $T1_{blood}$ (owing to the CA) to make the $2e^{-TI/T1_{blood}}$ term vanish, an expression for CBV can be formulated [49]:

$$CBV = 100 \cdot \frac{1}{\rho} \cdot \frac{S_{post} - S_{pre}}{A \cdot C_{blood}} \cdot \frac{1}{K_{slices}}. \quad (28)$$

The brain density is included to obtain CBV values in the familiar unit of ml/100 g, and K_{slices} is a factor that corrects for the fact that the optimal TI can be obtained only in one slice. K_{slices} can be calculated according to $K_{slices} = 2e^{-TI_{slice}/T1_{blood}}$ using literature values of T1 of blood and a TI_{slice} value that needs to be determined for the specific pulse sequence [49]. Two different approaches to find A and C_b are described and evaluated by Lu et al. [49]. Using the first approach, literature values of C_b are used and A is measured in cerebrospinal fluid (CSF) in a proton density weighted image. The second approach is based on estimation of $A \cdot C_b$ in a voxel with pure blood in the post-CA VASO image. In the work described in Paper I, the second approach was used, because it requires no additional proton density weighted scan, and the undesired CA-induced T2* effect in blood can be accounted for. However, according to Lu et al. [49], the first approach might provide results with better repeatability.

In a voxel containing only tissue, S_{post}-S_{pre} will be positive, because the TI of the IR sequence is chosen to cancel the blood signal component unaffected by CA, and T1 in the extravascular component is shorter compared to pre-CA blood. Thus, the signal from extravascular space is positive, both at the pre- and post-CA measurements, and the blood signal is positive in the post-CA situation and zero in the pre-CA measurement. However, for voxels containing components with long T1, predominantly CSF, the actual MRI signal can be negative for both the pre-CA and post-CA situations, and a positive contribution from blood can be interpreted as a decreased signal when studying the magnitude MRI images (showing absolute values), implying negative CBV estimates. To account for this effect, Lu et al. [49] used the absolute values of S_{post}-S_{pre}, which will be correct if both the pre-CA and post-CA signals have equal signs. In Paper I, an alternative method similar to that utilised by Uh et al. [50] was used to avoid problems in voxels where the sign of the MRI signal was changed by the CA. Hence, the phase of the MRI signal was used to elucidate whether the magnitude signal should be treated as positive or negative. Images from the VASO sequence, before and after CA administration, and a CBV map calculated according to Eq. 28 are shown in Fig. 5.

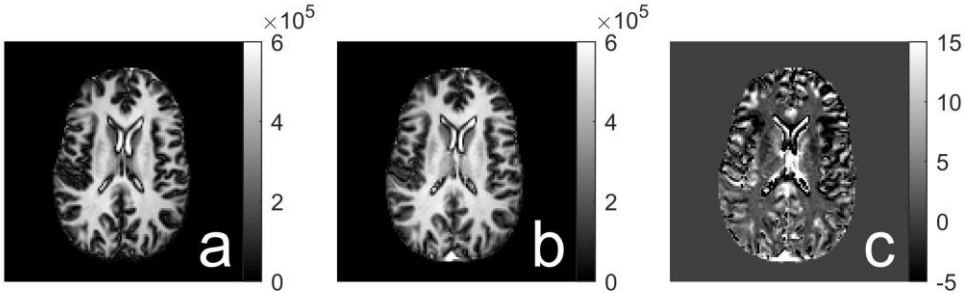

Figure 5. Images showing (a) VASO before CA administration, (b) VASO after CA administration, and (c) CBV. Note that in Paper I, CBV was calculated in regions of interest and no CBV images were obtained. Hence, the image above is displayed for visualisation purposes only, and no motion correction was applied. VASO images are shown in arbitrary (but comparable) units and CBV in ml/100 g.

4.6.3 Change in steady-state magnetic susceptibility

In Paper IV, an additional approach was introduced for steady-state CBV estimation. With this method, the fact that a paramagnetic CA would affect not only the relaxation times of the tissue but also the magnetic susceptibility was explored. The magnetic susceptibility of the material of interest influences the magnetic flux density B experienced by the spins in and around the object, and a change in B is reflected by a corresponding phase shift of the MRI signal, according to the Larmor equation. Hence, the MRI signal phase reflects the magnetic susceptibility, albeit in a rather complex manner, and the phase can be used to estimate the in vivo magnetic susceptibility. The procedure to convert phase information to quantitative susceptibility distributions (for arbitrary geometries) is called quantitative susceptibility mapping (QSM) and is discussed in detail in Chapter 7. If the susceptibilities of tissue and blood are known and the magnetic susceptibility change is assumed proportional to CA concentration, CBV can be estimated by comparing the change in susceptibility in tissue and in blood. Thus, when correcting for different haematocrit levels in large and small vessels, the expression for CBV is given by

$$CBV = 100 \cdot \frac{1}{\rho} \cdot \frac{1 - Hct_{LV}}{1 - Hct_{SV}} \cdot \frac{\left(\chi_{post} - \chi_{pre}\right)_{tissue}}{\left(\chi_{post} - \chi_{pre}\right)_{blood}}, \tag{29}$$

where χ_{pre} and χ_{post} represent the magnetic susceptibilities before and after (i.e. steady state) CA administration. Fig. 6 shows susceptibility maps and CBV calculated using Eq. 29.

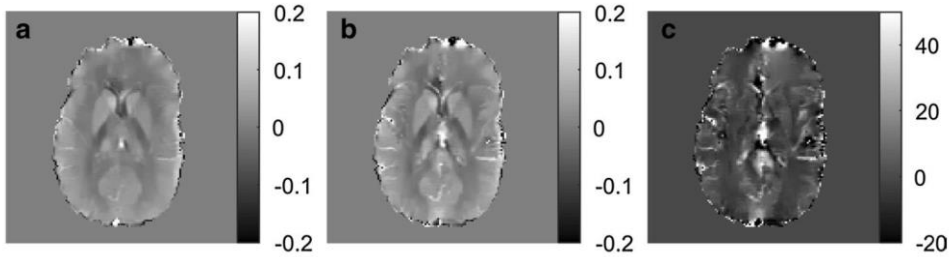

Figure 6. Images from Paper IV showing (a) magnetic susceptibility estimated using QSM before CA administration, (b) QSM image after CA administration, and (c) CBV. Susceptibility images are shown in ppm and CBV in ml/100 g.

5. Dynamic susceptibility contrast MRI

5.1 Tracer kinetic theory adapted to DSC–MRI measurement conditions

Dynamic susceptibility contrast MRI is a method to measure perfusion, based on the Meier–Zierler theory described in Chapter 3, employing Eqs. 13 or 20 to estimate CBF and Eqs. 16 and 19 to calculate CBV and MTT, respectively. However, some aspects should be further considered to adapt the theory to DSC–MRI.

The most common MRI CA consists of a Gd-chelate and, in the presence of an intact BBB, it remains in the vascular space while passing through the brain. The CA is situated in the blood plasma, and the plasma fraction differs between large vessels (used to define an arterial input function, AIF) and capillaries [7]. Hence, a correction factor is introduced to obtain the corresponding concentration of CA for whole blood. The correction is made by dividing the measured concentrations by the plasma fraction, approximated by (1-Hct), where Hct denotes the haematocrit level in the blood vessel of relevance. In most DSC–MRI experiments, haematocrit values from literature are used, often with assumed values of 0.45 in large vessels and 0.25 in small vessels [51], but methods for experimental estimation of in vivo haematocrit levels have been proposed [52].

As described in Chapter 3, R(t) is the fraction of the injected amount of tracer remaining in the volume at time t and, ideally, R(0) = 1. However, because R(t) is retrieved by a deconvolution of the concentration curves in tissue and blood, for experimental data, the estimated R(t) is not always strictly declining, because of, for example, imperfections in the mathematical deconvolution procedure [53] or the presence of arterial dispersion [54]. Hence, as an approximation, the maximal value of $R_{Sc}(t)$ is often used instead of $R_{Sc}(0)$ to find perfusion information [55].

With the above-mentioned DSC–MRI considerations, and using the common abbreviations for perfusion measurements in brain (i.e. CBF, CBV, and MTT), Eq. 13 can be written in the form

$$C(t) = \frac{\rho(1-Hct_{SV})}{(1-\mathrm{Hct_{LV}})}\mathrm{CBF}[AIF(t) \otimes R(t)]. \quad (30)$$

Thus, a deconvolution of the measured concentration curve in tissue, C(t), and in blood, AIF(t), results in the residue function scaled by CBF and the haematocrit constant, (i.e. $R_{Sc}(t) = CBF\rho(1 - Hct_{SV})/(1 - Hct_{LV})R(t)$), and CBF is approximated by the maximum value of $R_{Sc}(t)$. Alternatively, CBF can be estimated as

$$CBF = \frac{(1 - Hct_{LV})}{\rho(1 - Hct_{SV})} \frac{\max(R_{Sc}(t)) \cdot \int_0^\infty C(t)dt}{\int_0^\infty AIF(t)dt \cdot \int_0^\infty R_{Sc}(t)dt}. \quad (31)$$

Similarly, CBV and MTT are given by Eqs. 32 and 33, respectively.

$$CBV = \frac{(1 - Hct_{LV})}{\rho(1 - Hct_{SV})} \frac{\int_0^\infty C(t)dt}{\int_0^\infty AIF(t)dt}, \quad (32)$$

$$MTT = \frac{\int_0^\infty R_{Sc}(t)dt}{\max(R_{Sc}(t))}. \quad (33)$$

In Fig. 7, typical examples of CBF, CBV, and MTT images from a DSC–MRI experiment are shown.

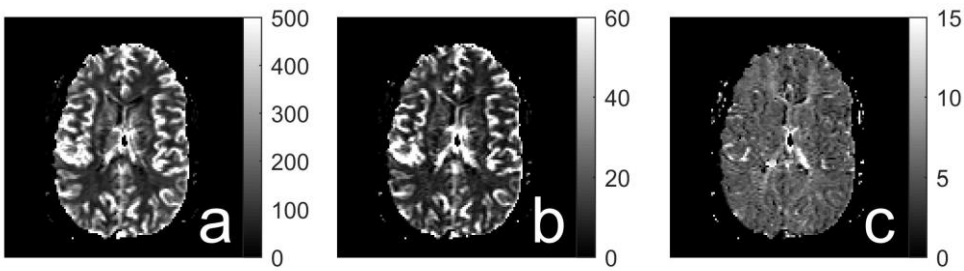

Figure 7. Images resulting from a standard DSC–MRI experiment showing (a) CBF (in ml/min/100 g), (b) CBV (in ml/100 g), and (c) MTT (in s) in a healthy volunteer.

5.2 Measurement considerations

As indicated by Eqs. 30–33, perfusion imaging requires concentration versus time curves in tissue and in an artery feeding the tissue of interest with blood. It is desirable to create a narrow bolus of CA to increase the contrast-to-noise ratio (CNR) [56]. Because the DSC–MRI CA is injected into an arm vein, the CA

travels through the heart, lungs, and heart again before it arterially enters the brain tissue of interest. This path of transport contributes to an inevitable temporal smearing of the bolus. To reduce temporal smearing or dispersion, it is desirable to use a high CA injection rate. For the same amount of injected tracer, a CA preparation with high molarity (implying a smaller total volume of CA) and a high injection rate will contribute to a short injection time. In the projects reported in this thesis, a CA preparation of 0.5 M [Dotarem, Guerbet, Paris, France] and an injection speed of 5 ml/s was used, which can be considered a standard procedure, creating a sufficiently short bolus [57].

It has been discussed whether to use spin echo (SE) or gradient echo (GRE) sequences to obtain the optimal information for perfusion imaging. It is recognised that SE sequences are selectively more sensitive to vessels with sizes of the same order of magnitude as the capillaries, implying that the response to the CA per unit of concentration, measured in terms of $\Delta R2$, is higher for small vessels [58]. For GRE sequences, the response, measured in terms of $\Delta R2^*$, is almost independent of the vessel size [59] but the overall sensitivity (i.e. transverse CA relaxivity) is higher. Thus, the choice of sequence will influence the resulting perfusion images. At a given concentration level, the effect on the MRI signal is more pronounced in GRE, leading to a higher CNR. At first glance, it would also seem reasonable to conclude that GRE is better for absolute quantification, owing to the fact that capillaries and arteries, contrary to the SE case, show more or less the same sensitivity (cf., Eqs. 31–32). However, this is not necessarily true, because this issue is complicated by the complex relaxivity situation in vivo, as further discussed below.

Another important basic parameter in the DSC–MRI data collection is the echo time (TE). As TE increases, the signal drop caused by the CA will be larger. However, simultaneously, the SNR of the baseline (i.e. the signal before the arrival of CA) is reduced. A high SNR at baseline has been shown to be advantageous in creating high quality perfusion maps. Thus, a rather short TE is preferable [56]. As a compromise between high baseline SNR and sufficiently large CA-induced signal drop in tissue, a TE of 29 ms was used in the studies described in this thesis.

For accurate quantification, the shapes of the concentration curves should be registered, and a high temporal resolution is thus a prerequisite for accurate perfusion images, particularly for AIF registration [56]. The temporal resolution in the studies reported in this thesis was 1.24 s. To obtain high temporal resolution together with sufficiently high spatial resolution and volume coverage, echo-planar imaging (EPI) readout is normally utilised in DSC–MRI.

5.3 Estimation of CA concentration from MRI signal

In DSC–MRI, the concentration of CA must be calculated from the MRI signal. Alternative methods for CA concentration estimations are discussed in this thesis and were addressed in Papers IV and V. However, in standard DSC–MRI, the change in transverse relaxation rate (i.e. ΔR2* for GRE-based imaging) is used. GRE images are collected before, during and after the passage of CA, and ΔR2* is calculated for each time point according to Eq. 34 (assuming pure T2*-weighting without competing T1 effects [60]).

$$\Delta R2^*(t) = -\frac{1}{TE} ln\left(\frac{S(t)}{S_0}\right), \tag{34}$$

where S(t) is the MRI signal at each time point, t, during the dynamic scan, and S_0 represents the baseline signal. The relationship between CA concentration and ΔR2* can, to a first approximation, be described as

$$\Delta R2^*(t) = r2^* \cdot c(t), \tag{35}$$

where r2* is the relaxivity of the CA, often considered to be a CA-specific constant. Thus, in most standard DSC–MRI experiments, the relationship between ΔR2* and CA concentration is assumed to be linear (i.e. r2* is a constant), and r2* is assumed identical for all tissue types and in blood. Thus, because calculation of perfusion parameters is based on the tissue-to-blood ratio of ΔR2* (cf. Eqs. 30–33), the exact value of r2* is not needed, because it cancels out in the calculations. Thus, the CA concentration in the equations needed for calculations of perfusion parameters is often replaced by ΔR2*.

Whereas Eq. 35 describes a simple relationship between ΔR2* and CA concentration, many methodological complications in DSC–MRI are attributed to the issue of quantifying CA concentration. Although the assumption of a linear response to the CA was predicted to be valid in brain tissue, for GRE data [61], the ΔR2*-versus-concentration relationship in whole blood is best described by a quadratic function [62,63]. Additionally, for the same concentration of CA, the transverse relaxation effect of CA has been shown to be much stronger in tissue [61,64], leading to, in relative terms, an underestimated AIF when the relaxivities in tissue and blood are assumed to be the same. The reason for the high relaxivity in tissue is that the CA shows a heterogeneous spatial distribution. The CA, residing in the intravascular space only, creates very strong field inhomogeneities, which extend to the extravascular compartment, and the spins outside the capillaries are effectively dephased [61].

Other issues related to the quantification of CA are predominantly associated with the AIF. Because the mean concentration of CA in blood is much higher than in the tissue compartment, it is difficult to find an optimal combination of CA dosage and TE that provides sufficient signal drop in tissue without simultaneously extinguishing the signal in blood completely, at maximal concentrations [19]. This phenomenon is often called the signal saturation or signal clipping effect. Thus, the shape of the AIF is affected, and this phenomenon is one reason for distorted peaks of the AIF concentration curves at high concentrations. In the study described in Paper II, to avoid this problem, an additional MRI pulse sequence with short TE was executed while a lower dose of CA was injected prior to the main bolus experiment (i.e. a prebolus). This prebolus scan was thus used only to collect blood signal data.

Another important problem often ignored or neglected in DSC–MRI is that the MRI signal originating from blood may be displaced at high CA concentrations because of local geometric distortions caused by susceptibility effects [65]. EPI readout is normally utilised to obtain high temporal resolution, and EPI is associated with very low bandwidth in the phase direction. At high CA concentrations, the magnetic susceptibility in blood is strongly increased, creating a frequency shift of the MRI signal, leading to a displacement of the signal in the phase encoding direction. Thus, when a given image pixel is used to trace the concentration during the time series, the blood signal may move out of the selected pixel of interest. This phenomenon can also contribute to distorted AIF curves at maximal concentrations. To optimise the information obtained from blood, a segmented EPI with higher phase direction bandwidth was used in Paper II for the prebolus experiment.

Another major difficulty in finding an accurate AIF is PVEs. With the spatial resolution usually achieved in DSC–MRI with the diameter of the arteries to be considered as an AIF candidate, there will, in practice, be no or very few voxels available with signal from only arterial blood [66,67]. All selected AIFs will thus be more-or-less influenced by PVEs, affecting both the shape and time integral, i.e. the area under the curve (AUC), of the AIF, and thus the quantitative estimates of the perfusion parameters. In a voxel with two different compartments (i.e. blood and tissue), the summed MRI signal is based on the addition of two vectors in the complex plane. It was demonstrated by van Osch et al. [67] that, when the CA passes through the voxel, a trajectory is created, forming a spiral-like path in the complex plane, with the origin of the spiral located at the tip of the tissue signal vector (see Fig. 8). Thus, the final shape of the AIF depends on where the sum of the two vectors ends up. Thus, for some concentration levels, the complex sum of the two vectors can be close to zero, corresponding to an apparently high CA concentration. Because of this effect, it is possible to estimate apparently higher concentration levels in an AIF from a pixel with PVEs than from a pixel consisting of blood only, and even a pixel with only small PVEs can substantially influence

the shape of the AIF [68]. It has also been shown that the impact of AIF PVEs on the resulting CBF levels, after the deconvolution procedure, is higher when the expected maximal signal drop is larger [68].

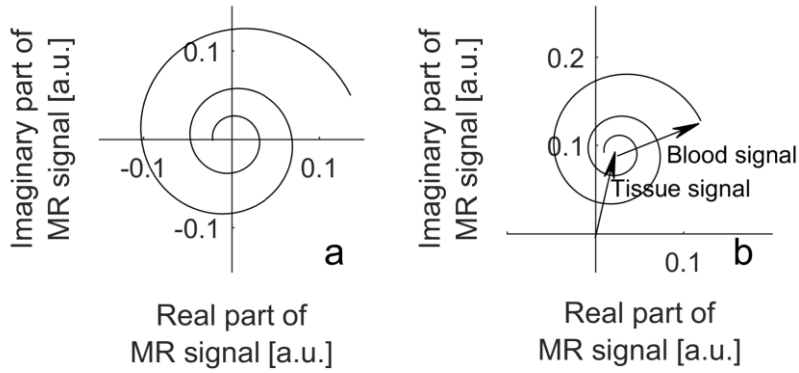

Figure 8. (a) Illustration of the signal during the passage of CA in a voxel containing only blood and (b) the addition of signal vectors from surrounding tissue and blood in the complex plane during the passage of CA, creating a spiral around the tip of the tissue vector. The theoretical explanation for the shape of the curves is given by van Osch et al. [67].

One additional phenomenon that can affect the estimated CA concentration based on $\Delta R2^*$ is the competing effect on the signal caused by the CA-induced change in longitudinal relaxation time, T1. Because the T1 is shortened by the CA, the MRI signal will tend to increase when the pulse sequence is not purely T2*-weighted. This will thus counteract the MRI signal decrease caused by the shortened $T2^*$. If a single-echo MRI sequence is used, and ΔR2* is calculated according to Eq. 35, a decreased T1 value may lead to some degree of ΔR2* underestimation. However, with a fairly long TR and a small flip angle, effects of shortened T1 caused by the CA can be minimised [69].

Another effect that can influence the estimated concentration levels occurs in situations where there is leakage through the BBB (e.g. in tumours). For such cases, the T2* relaxation effects of the CA are reduced, and T1 in the extravascular space are shortened [1]. The combined effect of changes in T1 and T2* in the presence of CA leakage can lead to either over- or under-estimated CBV values [60,70]. It is, however, possible to reduce the effects of leakage by injecting a small dose of CA before the DSC–MRI experiment [1] or by using post-processing correction methods [71-75].

5.4 Deconvolution

As described above, deconvolution of the tissue concentration curve with the AIF is required to obtain CBF and MTT. Because deconvolution is an ill-posed inverse problem that is noise sensitive, several studies have aimed at developing improved methods and to find the optimal deconvolution approach for DSC–MRI data [55,76-80]. Generally, deconvolution methods can be categorised into model-dependent and model-free methods. In the model-dependent approach, the residue function is described by an analytic expression. In DSC–MRI, it is most common to use model-free algorithms, where the output of the deconvolution (i.e. the tissue residue function scaled with the CBF) can assume any shape [60].
For practical situations, the measured AIF and the measured tissue concentration curve are discretised to a limited temporal resolution, and the convolution described in Eq. 30 can be expressed in discrete form as

$$\mathrm{C}(\mathrm{t_j}) \approx \frac{\rho(1-\mathrm{Hct_{SV}})}{(1-\mathrm{Hct_{LV}})} \cdot \Delta\mathrm{t} \cdot \mathrm{CBF} \sum_{i=0}^{j} AIF(t_i) \cdot R(t_j - t_i), \tag{36}$$

where the temporal sampling interval is denoted Δt, and the index, j, is used in the summation over different points in time. Several techniques exist to solve this equation, where methods, based on singular value decomposition (SVD) [55], are most commonly used in DSC–MRI [60].

For a short description of the SVD deconvolution method, the equation above can be formulated in matrix form as $\boldsymbol{c} = \boldsymbol{AIF} \cdot \boldsymbol{r}$ (including the constants in the matrices). Hence, to obtain $\boldsymbol{r}$, one needs to calculate $\boldsymbol{r} = \boldsymbol{AIF^{-1}} \cdot \boldsymbol{c}$. However, because AIF cannot always be inverted (i.e. the matrix is singular), the **AIF** matrix is decomposed into three matrices and $\boldsymbol{c} = \boldsymbol{U\Sigma V}^{\mathrm{T}} \cdot \boldsymbol{r}$, where $\boldsymbol{U}$ and $\boldsymbol{V}$ are orthogonal matrixes. T denotes the transpose operator, and $\boldsymbol{\Sigma}$ is a diagonal matrix with non-negative values. Thus, $\boldsymbol{r}$ can be obtained by solving $\boldsymbol{r} = \boldsymbol{V\Sigma^{-1}U}^{T}$. However, the residue function obtained from solving this matrix equation frequently suffers from severe oscillations, and to obtain a physiologically meaningful residue function, a threshold is applied to the singular values in $\boldsymbol{\Sigma}$. To avoid very high values in the inverted diagonal matrix, $\boldsymbol{\Sigma^{-1}}$, the threshold is applied, such that $\boldsymbol{\Sigma^{-1}}$ values are set to zero when the corresponding $\boldsymbol{\Sigma}$ value is below a certain threshold.

The early type of implementation, sometimes referred to as standard SVD, is sensitive to time shifts of the data (see Section 5.5). A modified method, called block-circulant SVD deconvolution [79], was soon developed and is currently the most commonly used algorithm in DSC–MRI calculations. SVD deconvolution has become popular owing to its robustness and computational efficiency. For these reasons, the block-circulant SVD algorithm was used in the studies described

in Papers I–III and V. It should, however, be noted that the estimated CBF values tend to be underestimated with this deconvolution technique, particularly at low SNR and short MTTs [79].

For CBF and MTT estimations, only the maximum value and the integral of the impulse response function (R_{Sc}) is used. However, in some applications, it is particularly important for the deconvolution algorithm to return curves where the entire shape of the R_{Sc} curve is reliable. One such example is when R_{Sc} is used to study flow heterogeneity and distribution of transit times in attempts to assess oxygen extraction fraction (OEF) and cerebral metabolic rate of oxygen ($CMRO_2$) [81-84]

5.5 Arterial delay and dispersion

Two important additional issues in the perfusion estimation are arterial delay and arterial dispersion. The standard procedure is to use a global AIF for all tissue voxels, or, sometimes, a limited number of local AIFs [85-87], and some degree of time delay between the measured AIF and a given tissue concentration curve is likely to occur. Deconvolution algorithms, as mentioned above, can be sensitive to any time shift (positive or negative) between the AIF curve and the tissue curve. Thus, the deconvolution algorithm is sensitive to any time delay between the arterial curve at the AIF measurement site and the corresponding arterial curve at the inlet of the tissue, and, in standard SVD deconvolution, this leads to underestimated CBF and overestimated MTT (in the case when the tissue curve appears after the arterial curve) [88]. It is, however, possible to avoid the effects of delay, either by shifting the curves before deconvolution or, as mentioned above, to use a deconvolution algorithm that is delay insensitive, for example, the block-circulant SVD as was used in the studies of Papers I–III and Paper V.

A more severe effect caused by the difficulties in measuring the true AIF for each tissue voxel is a dispersion of the AIF curve that will take place when the CA bolus travels from the AIF measurement site to the inlet of the tissue voxel of interest. Ideally, the measured tissue concentration curve should reflect a convolution of the tissue impulse response function with the true AIF, but the true AIF is also a convolution of the measured AIF with a generally unknown dispersion function. This extra convolution, in the presence of dispersion, will affect the shape of the retrieved impulse response function, and dispersion effects will lead to underestimated CBF values and overestimated MTT [88]. Attempts have been made to characterise the dispersion by analysing the R(t) shape [77,89,90] and modelling the dispersion and incorporating it into the deconvolution procedure using, for example, the nonlinear stochastic regularisation approach [80]. Note that CBV is calculated as the ratio of the

measured tissue concentration time integral to the measured AIF time integral, and CBV is thus unaffected by both delay and dispersion effects, as long as the total measurement time is sufficiently long, because neither delay nor dispersion will alter the total amount of tracer molecules [88].

5.6 Absolute quantification of perfusion in DSC–MRI

Using standard DSC–MRI methodology and analysis, considerable overestimation of CBF and CBV is frequently seen. For example, in Paper I, the reported mean CBF estimate in GM was 277 ml/min/100 g using DSC–MRI (i.e. 4–5 times higher than the corresponding CBF values obtained by pCASL). Apart from potential deconvolution issues in the CBF quantification, the same errors affect the quantification of CBV and overestimations of the same order of magnitude as for CBF are often seen in CBV. One important reason for the overestimation is the problem of finding an AIF without PVEs. As was described earlier, PVEs can affect the AIF shape in many different ways, giving both over- and under-estimated concentration values. However, generally, the effect of PVEs leads to underestimated CA concentration values. Thus, overestimation of CBF and CBV occurs. In cases where special efforts have been made to correct for first-order arterial PVEs, by correcting or rescaling the AIF time integral, overestimations in CBV and CBF are often still of the order of a factor 1.5–2.5 [20,91]. This has often been attributed to the tissue-versus-blood relaxivity issue. However, in the prebolus DSC–MRI study described in Paper II, no remaining overestimation was observed after PVE correction. In this study, arterial PVEs were corrected by rescaling the AIF time integral with a venous output function (VOF) time integral, and the VOF was measured in a large vein using a small prebolus of injected CA before the normal DSC–MRI experiment.

As mentioned, the difference in transverse relaxivity between tissue and blood is likely to cause an overestimation of CBF and CBV, particularly at high magnetic field strengths. Because a given CA concentration will have a smaller effect on the transverse relaxation rate in blood compared to tissue, the concentration levels in blood will, relative to tissue, be underestimated in blood if the same relaxivity is assumed. Again, an underestimated AIF will cause overestimated CBF and CBV values. As reported in Paper V, it should be noted that, in a normal DSC–MRI experiment, the AIF is likely to be registered in a voxel with a substantial amount of PVEs. The relaxivity corresponding to such an AIF voxel can, as reported in Paper V, be very similar to the tissue relaxivity, estimated in the study reported in Paper IV and predicted by Kjølby et al. [61]. However, in the prebolus study described in Paper II, the resulting mean CBF value in GM was 55 ml/min/100 g, which is in good agreement with gold-standard

CBF techniques [9]. Hence, no overestimation related to different relaxivities in tissue and blood was detected, which is somewhat contradictory to other observations, considering that PVEs were minimised in this case. When PVEs are reduced, one would expect differences in relaxivity to manifest themselves more clearly.

5.7 Calibration of DSC–MRI data for perfusion quantification

For quantification of CBF in absolute terms, different approaches have been proposed for calibration of DSC–MRI data. One simple approach has been to use normal-appearing WM as a reference region [92], whereas others have suggested determining a general correction factor (CF) from a direct comparison between DSC–MRI data and a reference perfusion measurement method (e.g. PET), and to subsequently apply this general CF to all subjects [93]. None of these approaches is optimal, because, first, CBF in normal WM varies among different subjects [94], and, in second, the use of a general CF is problematic, because the sources of error (e.g. the amount of PVEs) show large individual variations [69]. It is thus highly recommended to use a subject-specific CF, preferably to be determined during the same scanning session as the DSC–MRI experiment [69].

CBF and CBV estimates are influenced by the same errors in the AIF time integral and will, thus, suffer from the same degree of overestimation. Thus, once either CBF or CBV is independently quantified, all three parameters estimated from DSC–MRI (CBF, CBV, and MTT) will be available in absolute terms. Obviously, deconvolution-related issues and large distortions in AIF shape (only relevant to CBF) may complicate this assumption. However, DSC–MRI-based MTT measurements tend to show similar absolute values as PET gold standard estimates [95,9]. These arguments imply that it is reasonable to apply a CBV-based CF for CBF corrections.

In the following section, different approaches to obtain a CF for CBF and CBV estimates originating from a standard DSC–MRI experiment are described. The CFs are generally used to obtain quantitative values in absolute terms according to

$$CBF = CBF_{DSC-MRI} \cdot CF, \tag{37}$$

$$CBV = CBV_{DSC-MRI} \cdot CF, \tag{38}$$

where CBF and CBV refer to the corrected values, given in absolute terms, and $CBF_{DSC\text{-}MRI}$ and $CBV_{DSC\text{-}MRI}$ are the uncorrected values.

5.7.1 Prebolus data used to rescale the arterial input function

As previously mentioned, the issue of arterial PVEs is one of the most pronounced problems in perfusion quantification using DSC–MRI. One promising approach is, as mentioned, to rescale the AIF by comparing the AUC of the AIF with a VOF from a large vein (e.g. the sagittal sinus, which is easy to locate and has a large diameter). However, in a standard DSC–MRI experiment, the VOF registration will also suffer from signal saturation and signal displacement in the same way as the AIF. In the study reported in Paper II, the VOF was measured using a pulse sequence optimised for blood signal only (i.e. sufficient effect of CA on the tissue signal was not required). Thus, data using a pulse sequence specifically adapted to VOF measurements were collected during the passage of CA following injection of a smaller dose (i.e. 20% of a normal single dose as in the study described in Paper II). This small CA dose was injected before the main DSC–MRI experiment and is thus referred to as a prebolus. The prebolus pulse sequence employed segmented EPI readout with high bandwidth to avoid blood signal displacement during the CA passage, and a shorter TE, which, with a lower dose of CA, assures that signal saturation at peak concentration can be avoided. After a simple correction for different CA doses, the AUC from a VOF (AUC_{VOF}) was then compared with the AUC of the AIF from the main bolus DSC–MRI experiment (AUC_{AIF}) to establish the CF according to

$$CF = \frac{AUC_{AIF}}{AUC_{VOF}}. \tag{39}$$

In Paper II, it can be seen that the prebolus approach for calibration of DSC–MRI data resulted in a mean GM CBF of 55 ml/min/100 g, which is close to corresponding values from PET measurements. Additionally, repeated experiments in the same subject on two separate occasions (test–retest) showed that the repeatability increased after calibration with the prebolus CF (see Fig. 9). This study indicated that the main quantification problem in DSC–MRI was related to arterial PVEs. Thus, it is somewhat surprising, considering the fairly well-established relaxivity difference between tissue and whole blood, as mentioned above.

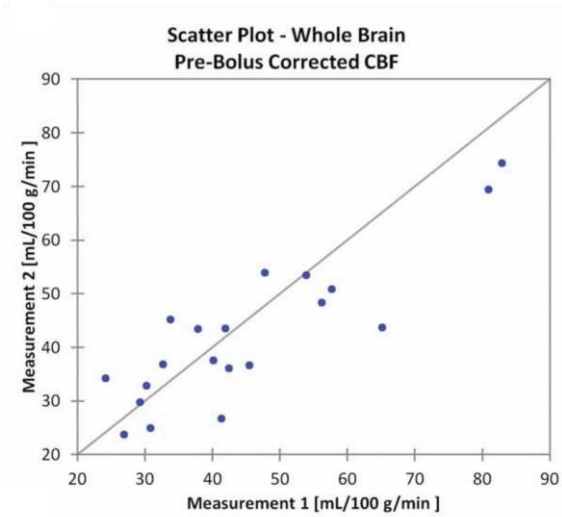

Figure 9. Scatter plot from Paper II, showing the test-retest results of whole-brain CBF values after calibration with the prebolus approach. The intra-class correlation coefficient was 0.85.

5.7.2 Tail-scaling correction of the AIF

Another approach for correcting the AIF for PVEs is to compare concentration values in the steady-state period (i.e. in the so-called tail of the concentration curve) from a standard AIF and a large-vein VOF from the same DSC–MRI experiment [76]. Thus, a CF can be estimated without the need for any additional data acquisition, and this CF can be described as

$$CF_{AIF} = \frac{C_{VOF}}{C_{AIF}}, \tag{40}$$

where C_{VOF} and C_{AIF} are the mean concentrations at steady state for the VOF and the AIF, respectively. CF_{AIF} is a correction factor, used for rescaling the AIF, before utilising it for perfusion calculations. Using this correction method, CBF and CBV estimates close to PET literature values were seen in a study performed with a double dose of CA (0.2 mmol/kg body weight) at 1.5 T [76]. However, the same method provided higher absolute values when performed at 3T [96] and 7T [97]. The mean CBF values in GM were 58 ml/min/100 g at 1.5T [76], 80 ml/min/100 g at 3T [96], and 114 ml/min/100 g at 7T [97]. However, in one study at 3T, the absolute levels of CBF and CBV were lower than values obtained at 1.5T [98]. One possible reason for the observed differences in absolute levels is an increased difference in relaxivity between tissue and blood with increasing field

strength, as predicted by Kjølby et al.[61]. However, the cause of the field strength-related differences is not yet fully established.

5.7.3 Calibration using an additional CBV measurement

One of the advantages of DSC–MRI is that CBF, CBV, and MTT can be estimated simultaneously. However, other methods to measure CBV with MRI exist, and because CBF is, at a first approximation, overestimated by the same factor as CBV, a CF for CBF can be found by comparing DSC–MRI CBV with an alternative CBV method as

$$CF = \frac{CBV}{CBV_{DSC-MRI}}. \tag{41}$$

Here, CBV denotes the estimate obtained by an alternative method. Alternative CBV measurements methods include the Bookend method, where the CA-induced change in T1 is used, and VASO, where a pulse sequence cancelling the signal from blood in the pre-CA situation is used. These CBV methods are described in more detail in Chapter 4. Principally, it would also be possible to use CBV measurements based on the CA-induced susceptibility difference, as was discussed in Chapter 4. The Bookend technique has been used in several studies, evaluating the repeatability and comparing the estimates to other methods. In the study reported in Paper I, the mean absolute level was in good agreement with ASL, but the repeatability of the CBV estimation from the T1 maps and the calibrated DSC–MRI CBF estimates was moderate (Fig. 10). Additionally, the direct comparison of corrected DSC–MRI CBF values with CBF from pCASL in GM failed to show good correlation between methods. However, in contrast to Paper I, other studies have shown good agreement with PET [99] and pCASL [100]. Repeatability data were reported by Shin et al. [48], including patients scanned with 123 ± 111 days between examinations, and by Crane et al. [98], analysing data from patients scanned a second time after 2–3 days. Shin et al. found reasonable repeatability, whereas Crane et al. showed a low but significant CBV correlation between the two scanning occasions only in some parts of the brain. One reason for the poor repeatability reported in Paper I might be lower-than-normal CA concentrations in the steady-state period because of a somewhat later execution of the post-CA T1 measurement. It is interesting to note that, in the repeatability study by Shin et al. [48], a double dose of CA was injected for some of the study subjects. Other Bookend studies used a single dose [21,45]. If the repeatability of one method is poor, it is problematic to obtain good agreement with another method. This might explain the moderate correlation with pCASL. In Paper I, similar results were reported for the VASO calibration approach, with moderate repeatability (Fig. 10)

and difficulties to find good correlation with CBF values from pCASL. However, Uh et al. [101] showed excellent repeatability and good correlation with PET values for CBV VASO estimates. The repeatability in that study was based on two subsequent VASO measurements during the same session (i.e. without repositioning of the subject). This is a significant difference compared with the study reported in Paper I, where the examinations were separated by at least 7 days. In contrast to the Bookend method, VASO measurements are favoured by a time delay between the CA bolus passage and data acquisition, because the effect of water exchange between the intra- and extra-vascular spaces is minimised. Uh et al. [50] showed that it is optimal to conduct the VASO experiment 7–14 min after the CA injection, and the time delay was approximately 9 min in the study in Paper I.

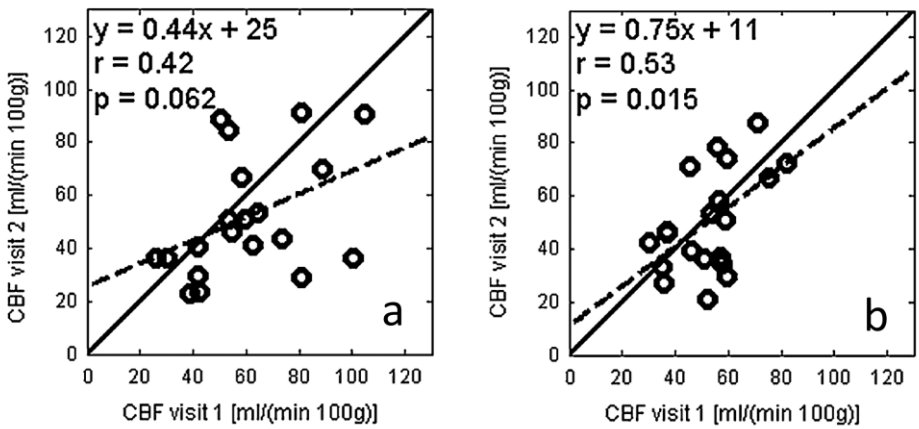

Figure 10. Scatter plots from Paper I showing test-retest results. The displayed results correspond to using a WM ROI for calibration purposes for (a) Bookend-calibrated CBF values and (b) VASO-calibrated CBF values.

5.7.4 Calibration using an additional CBF estimate

If CBF can be independently estimated in absolute terms using another MRI method, a patient-specific CF can be found in a similar manner. In such a case, the CF can be established as

$$CF = \frac{CBF}{CBF_{DSC-MRI}}, \tag{42}$$

where CBF is estimated using an alternative method to DSC–MRI.

One suggested method for alternative CBF estimates is ASL [102]. By using CBF information from ASL in regions with short bolus arrival times, realising that a long bolus arrival time is associated with inaccurate CBF values, a CF can be

determined and used to calibrate CBF and CBV maps from DSC–MRI. Using this approach, similar values as XeCT were obtained, and the correlation between calibrated DSC–MRI values and XeCT was higher than the correlation between ASL and XeCT in regions with long bolus arrival time. In a whole-brain CBF comparison between calibrated DSC–MRI and XeCT, the correlation was, however, moderate [102].

Another approach for finding CBF information using an alternative method is to measure the total CBF using phase-contrast MRI for flow quantification [103]. If the blood flow is measured in both the internal carotid and the vertebral arteries, the total supply of blood is measured, and a total CBF can be estimated. By comparing this measure to the total CBF from DSC–MRI, estimated by adding all pixels with GM or WM, a CF is obtained according to Eq. 42. Using this calibration approach, the variance of measured CBF values are reduced, compared to uncalibrated values [103].

6. Phase images and magnetic susceptibility

6.1 Basic theory and contrast mechanisms

The signal obtained in MRI, often described by a complex number, is related to the local magnetisation vector of the object. In the image reconstruction, the most common approach is to visualise a value proportional to the length or absolute value of the complex signal vector in magnitude images. The magnitude of the signal depends on the settings of the MRI scanner in terms of the selected mode of weighting (e.g. TE, repetition time, flip angle), the proton density and relaxation parameters of the tissue and on proportionality constants related to the hardware. However, by studying the phase of the signal, additional information can be obtained, because the measured phase shift, corresponding to the frequency shift relative the resonance frequency, ν_0, reflects the difference in magnetic flux density (relative B_0) experienced by the spins, according to the Larmor equation.

$$\Delta\phi = \gamma \cdot \Delta B_z \cdot TE. \tag{43}$$

Here, ΔB_z is the deviation in magnetic flux density (in tesla) from the main magnetic flux density, B_0, assumed to be directed along the z-axis, γ is the gyromagnetic ratio ($2\pi \cdot 42.6$ MHz/T for hydrogen) and TE is the echo time. Below, the more general term, 'magnetic field' is sometimes used in connection with descriptions of magnetic flux density.

Phase images can be used to enhance the contrast in magnitude images, as in susceptibility-weighted imaging (SWI) [104,105], to explore new tissue contrast patterns [106-108], to quantify the magnetic susceptibility to study tissue properties [109] and to estimate the concentration of a paramagnetic CA [110]. Another common application for MRI phase imaging is to study spins moving in a magnetic field gradient (e.g. to obtain information about flow [111-113]), as mentioned in Section 5.7.4.

In the context of this thesis, the use of phase maps for the assessment of magnetic field variations is of particular relevance. When an object is placed in an external magnetic field, it becomes magnetised to a degree that depends on the

magnetic susceptibility of the material. For a homogenous substance, the magnetic susceptibility is a scalar, specific for each material, and it can be either positive or negative. Both paramagnetic and ferromagnetic materials show positive susceptibility, with a much higher (non-constant) susceptibility for ferromagnetic materials. Materials with negative magnetic susceptibility are called diamagnetic [114]. However, it has been shown that, for some materials, the magnetic susceptibility is best described by a tensor, because it depends on geometry and differs between different angles relative to the external magnetic field [115]. For brain tissue, this effect is most pronounced in WM, where the anisotropy in the susceptibility is predominantly caused by the lipids in myelin [116]. However, the research concerning anisotropic susceptibility is ongoing and, in most cases, the magnetic susceptibility is approximated by a scalar, as was done in the studies described in Papers IV and V.

Whereas phase information is used mostly for calculating parametric maps, the phase image itself can offer a unique contrast pattern, because the phase reflects the underlying magnetic susceptibility [106-108]. In the brain, the magnetic susceptibility is diamagnetic, because of the overabundance of water and different levels of iron, myelin, and calcium [117], which affect the susceptibility to make it slightly more paramagnetic or diamagnetic. The main source of magnetic susceptibility contrast in GM is iron, whereas the main source of contrast in WM is assumed to be myelin [118].

6.2 Relationship between magnetic field and susceptibility: the general case

In the MRI unit, the resulting magnetic field depends on both the magnetic susceptibility and the geometry of the object of a given material. For the general case, the induced change in magnetic flux density, ΔB_z, relative the magnetic flux density of the main magnetic field, B_0 (along the z direction), is described by a convolution of the susceptibility distribution and a unit dipole kernel [119,120].

$$\Delta B_z(r) = B_0 \cdot \frac{3\cos^2\theta - 1}{4\pi r^3} \otimes \chi(r). \tag{44}$$

Here, θ is the angle relative to the main magnetic field, r is the position given in spherical coordinates and χ(r) is the spatial distribution of the magnetic susceptibility. Hence, the kernel, $(3\cos^2\theta - 1)/4\pi r^3$ in Eq. 44, is the unit dipole. Eq. 44 can also be described in the Fourier space as [121-123].

$$\Delta B_z(r) = B_0 \cdot FT^{-1}\left[\left(\frac{1}{3} - \frac{k_z^2}{K^2}\right) \cdot FT\big(\chi(r)\big)\right]. \quad (45)$$

In Eq. 45, the unit dipole is expressed in Fourier space, where $\boldsymbol{k}$ is the k-space vector, k_z, the coordinate in the direction of the main magnetic field and $K = \sqrt{k_x^2 + k_y^2 + k_z^2}$ gives the magnitude of $\boldsymbol{k}$. The direct relationship between the magnetic field difference, which can be measured using phase imaging according to Eq. 43, and the susceptibility distribution enables a method for quantification of relative magnetic susceptibility using MRI. This method is often referred to as QSM and is further discussed in Chapter 7.

6.3 Relationship between magnetic field and susceptibility: the cylindrical object

For some specific geometries, it is possible to express the relationship between the magnetic field and the susceptibility in an explicit analytical form. The solution of Eqs. 44–45 for $\chi(r)$, by deconvolution, is an ill-posed inverse problem. It is sometimes useful to apply simpler equations for specific geometries. For a cylinder, the solution is well known and is commonly used to characterise the phase shift in and around blood vessels [124-129]. The magnetic flux density inside the cylinder, ΔB_{in} (relative B_0), is described by [114].

$$\Delta B_{in} = \frac{\Delta\chi}{6}(3\cos^2\theta - 1)B_0 + \frac{1}{3}\chi_{out}B_0. \quad (46)$$

Here, χ_{out} is the magnetic susceptibility outside the cylinder, $\Delta\chi$ is the difference between the internal and the external susceptibility ($\Delta\chi = \chi_{in} - \chi_{out}$), B_0 denotes the main magnetic field and θ is the angle between the long axis of the cylinder and the direction of the main magnetic field, as shown in Fig. 11. Eq. 46 was also used in Paper IV to estimate susceptibility in a blood vessel.

The magnetic flux density (relative B_0) outside the cylinder, created by the cylinder, ΔB_{out}, can be expressed as [114]:

$$\Delta B_{out} = \frac{\Delta\chi}{2}\frac{a^2}{d^2}\sin^2\theta\, cos2\Phi B_0 + \frac{1}{3}\chi_{out}B_0. \quad (47)$$

Here, a is the radius of the cylinder, and d and Φ are coordinates describing the position outside the cylinder according to Fig. 11.

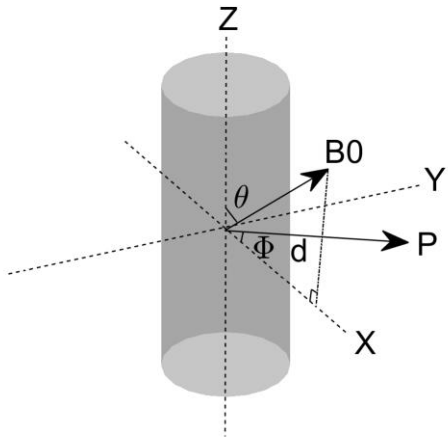

Figure 11. Illustration of a cylinder placed in a magnetic field B_0. θ is the angle between the long axis of the cylinder (Z direction) and the main magnetic field, d and Φ describe the xy-plane position of the point P where the magnetic field is calculated outside the cylinder.

The magnetic field shift inside the cylinder depends on the angle of the cylinder relative to the direction of the main magnetic field (B_0), and both an increase and a decrease of the magnetic flux density can be observed, depending on the orientation of the cylinder. Thus, for a blood vessel with higher susceptibility than the surrounding tissue (i.e. positive $\Delta\chi$), an increased magnetic field, compared to surrounding tissue, is to be expected if the blood vessel is oriented parallel to the main magnetic field. However, a decreased magnetic field is expected for a blood vessel oriented perpendicular to B_0. Similarly, an increase in CA concentration, which increases susceptibility, can lead to increased or decreased magnetic field, depending on the orientation of the cylinder relative to the main magnetic field. Profiles across the diameter of a cylinder with different orientations relative the main magnetic field are shown in Fig. 12.

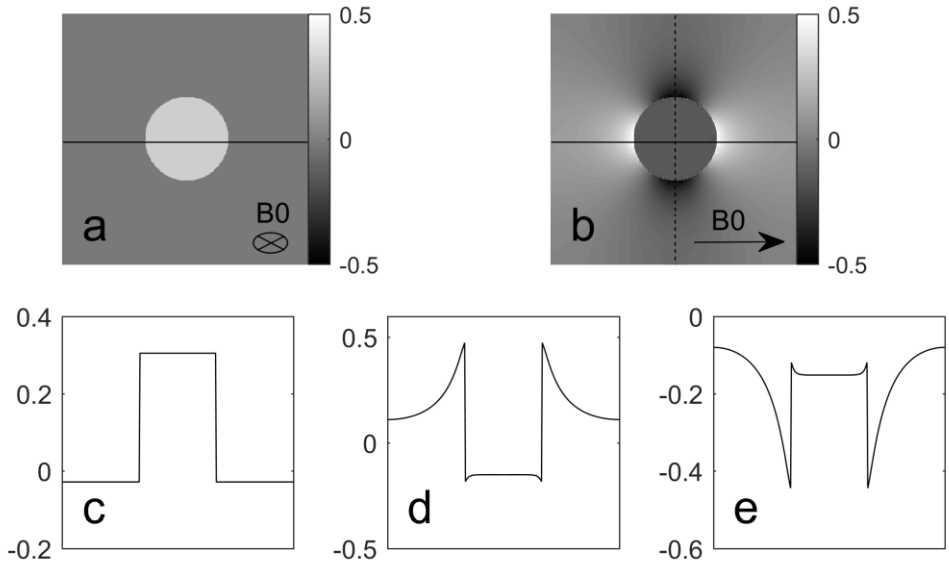

Figure 12. Simulated phase images and profiles showing the magnetic field shift created by the cylinder. Phase images are shown in radians for a cylinder placed (a) parallel and (b) perpendicular to the main magnetic field. Profiles are drawn perpendicular to the long axis of the cylinder for the case of a cylinder placed (c) parallel to the magnetic field (profile indicated by the solid line in (a)), (d) perpendicular to the magnetic field (profile indicated by the solid line in (b)) and (e) perpendicular to the magnetic field (profile indicated by the dashed line in (b)). The difference between (d) and (e) is that the profile is drawn (d) parallel to the main magnetic field and (c) perpendicular to the main magnetic field. The y-axes in (c)–(e) show the geometry factor (i.e. for the actual magnetic field shift, the values should be multiplied by $\Delta\chi$ and B_0).

6.4 Post-processing of phase images

Phase images are, in this context, used to obtain information about the magnetic field shift caused by the magnetisation of tissue with a given magnetic susceptibility, as described above. However, when an object is placed in the uniform magnetic field of an MRI scanner, the magnetic field in a voxel will be affected not only by the susceptibility inside the voxel, but also by the susceptibility of all surrounding voxels in and around the tissue. In fact, the most pronounced effect on the total magnetic field is caused by the effect of air surrounding the object, provided that the susceptibility difference is large, as is normally the case when the object of interest shows susceptibility levels close to tissue water. Hence, when visually inspecting a phase image prior to any post-processing, the most pronounced impression is a slowly and smoothly varying phase throughout the whole object. This contribution to the total magnetic field is often referred to as the background field. The phase values are displayed in an interval from zero to 2π, and when a magnetic field variation in an object is large enough to create frequency variations corresponding to phase values exceeding 2π

at a given TE, the phase map will display phase wraps. The post-processing steps to obtain useful field maps are described below, and examples of the image appearance through the post-processing procedure are shown in Fig. 13.

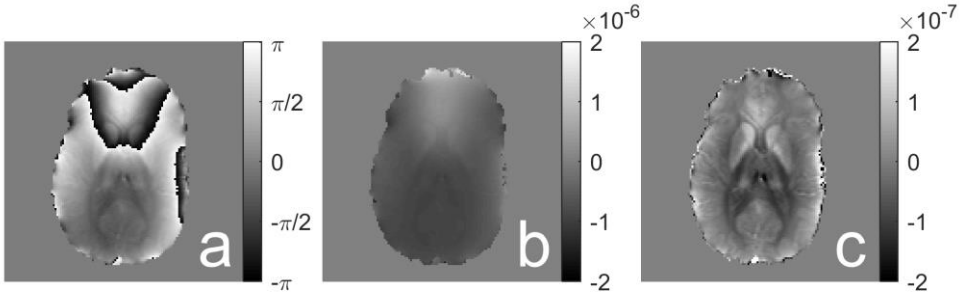

Figure 13. Images at different steps in the process of phase image post-processing. (a) Original phase image, including phase wraps (in units of radians), (b) unwrapped phase image converted to the field difference in units of T (according to Equation 43) with remaining background field contributions, and (c) the field difference after unwrapping and removal of background field (in units of T).

6.4.1 Unwrapping

To obtain the phase values actually reflecting the magnetic field (i.e. values outside [0, 2π]), the phase image should be unwrapped. Unwrapping can be accomplished by different methods, using a number of different algorithms, either in the temporal or in the spatial domain. If a multi-TE MRI sequence is used, temporal unwrapping can be utilised, in which the phase is unwrapped by comparing phase values at different TEs in a single pixel. For such methods, multiple phase wraps must be avoided between subsequent TEs. Hence, a sufficiently short inter-echo time is needed, and this can be a challenge at high magnetic fields, because ΔB_z, and thereby the phase shift, for a given susceptibility level increases with B_0 according to Eqs. 44–45 [117].

For spatial unwrapping, several different techniques exist, in which the phase values of neighbouring pixels are compared [117]. One of these methods, utilising a path-tracking algorithm [130], was used in the studies reported in Papers IV and V. Using this method, phase values of adjacent voxels are compared, and an integer times 2π is added if the difference between the voxels is larger than π. Thus, one starts with a reference pixel and the pixel neighbours are evaluated in a step-wise manner, creating a path. If one voxel is incorrectly assessed, the rest of the path will be misinterpreted. The risk for incorrect assumptions increases with noise. Hence, to avoid such effects, the noisy parts are evaluated last in the unwrapping process.

For the unwrapping to work, the true phase difference between two neighbouring pixels should be less than π [117,130]. This condition is not always fulfilled for long TEs and for regions having large spatial variations in magnetic

susceptibility. This problem was identified for data reported in Papers IV and V, and the unwrapping tended to fail in regions close to the sinuses and in large veins, such as the sagittal sinus. Hence, manual unwrapping was performed by adding or subtracting multiples of 2π in these regions. As an approximate angle of the sagittal sinus relative to the main magnetic field can be determined at different locations in the brain, and the susceptibility difference between the vein and the surrounding tissue is approximately known, it was possible to manually assess whether any additional unwrapping was required. The use of an additional manual unwrapping is, however, not ideal, because it is time consuming and imposes a risk of user dependence in difficult areas. The only reason for using it was that the phase images from a standard DSC–MRI experiment were used. In future studies, it would be beneficial to use multi-echo data with short inter-echo times to avoid large phase differences between neighbouring voxels.

For dynamic measurements, with gradually varying CA concentrations, as in a DSC–MRI or DCE–MRI experiment, an alternative unwrapping approach can be used called pairwise subtraction [131]. In this procedure, a complex signal representation is expressed using the phase information as $Z_j = \exp(i\phi_j)$, and the phase difference between two adjacent time points on the dynamic curve is given by

$$\Delta\phi_t = \Delta\phi_{2/1} + \Delta\phi_{3/2} + \cdots . + \Delta\phi_{j/(j-1)} + \cdots . + \Delta\phi_{t/(t-1)}, \qquad (48)$$

where $\Delta\phi_{j/(j-1)} = \arg(Z_j/Z_{j-1})$. This method requires that the phase difference between two adjacent time points, for all time points, is restricted to be in the interval of $-\pi$ to π, which is likely to be fulfilled if a high temporal resolution is used [131]. This method was successfully applied to unwrapping of phase images in the $\Delta\phi$ versus time curve in the study described in Paper III.

6.4.2 Removing background phase

To assess information about magnetic field components created by sources inside the volume of interest, the background field must be removed. Several techniques exist, including high-pass filtering, geometry-dependent artefact correction, sophisticated harmonic artefact reduction for phase data (SHARP), the Laplacian boundary value (LBV) method, the projection onto dipole field (PDF) approach, and several others [117,132-134].

The most straightforward method is to use a high-pass filter to remove the background field. This method is common in applications where the quantitative values of the phase are not important (e.g. SWI). Regarding such filters, it is, however, difficult to establish the optimal filter size, because a small filter size

might not succeed in removing the entire background field, whereas a larger filter size might remove some of the desired information [133].

The geometry-dependent artefact correction method is based on segmentation of the image into two categories: tissue and air. The segmented image is then used to estimate the magnetic field originating from the tissue-air distribution. After removing the estimated tissue/air dependent magnetic field, an additional high-pass filter is applied to take other undesired phase components into account, for example, contributions from eddy currents. The additional high-pass filter needed is, however, far less aggressive, and will remove less of the desired phase information, compared to using only a high-pass filter to remove background field contributions [132,135].

In SHARP, the background field is removed from the total field by assuming that the field created from sources in the background are harmonic, whereas the magnetic field created by sources inside the volume of interest is non-harmonic [117,136].

In LBV, the Laplace equation for the background field can be solved by assuming that the total field at the boundary of the ROI originates from the background field only. This is a reasonable approximation, because the contribution from the background field is normally one or two orders of magnitude higher than the magnetic field contribution from sources inside the object [134,137].

In the studies reported in Papers IV and V, PDF was employed to remove undesired phase contributions, and this is a method that utilises the fact that the field created by dipoles outside the ROI is approximately orthogonal to the field created by dipoles inside the ROI [117,134,138]. Hence, if the total measured field is projected to the space spanned by fields created by all possible susceptibility distributions outside the ROI, the contributions from the field from sources inside the ROI will be eliminated [117,134,138]. The result from the projection operation is thus a field map showing only contributions from the background field. To obtain the desired field created by sources inside the ROI, the result from the projection operation needs to be subtracted from the total measured field [117,134,138]. In Papers IV and V, PDF was shown to generate phase images with appealing visual appearance without obvious artefacts.

It has been shown by other groups that PDF provides accurate results, similar to other comparable background removal methods, inside the ROI [139]. However, close to the boundary of the ROI, the assumption of orthogonality does not hold, and the phase values obtained at the boundary are associated with considerable uncertainty [138]. Problems associated with this issue were only expected to have a small effect in the study of Paper V, in which only tissue data were registered close to any boundaries, and the boundary part of the tissue constituted only a small fraction of the total ROI for grey or white matter of the whole brain. The same argument is valid for tissue data in Paper IV. However, in Paper IV,

information about blood susceptibility before and after CA administration in the sagittal sinus was also required. The sagittal sinus is situated close to the air-tissue boundary, and to avoid uncertainties caused by the PDF algorithm, susceptibility was instead estimated by recording phase values from images with background contributions, followed by calculation of the susceptibility for a cylinder according to Eq. 46. In future studies, if the sagittal sinus is to be used for susceptibility information, LBV background removal might be a better choice, because it has been shown to provide more accurate values close to boundaries of the ROI [135].

In Paper III, there was no need for removing the background field, because only a small region of the image was analysed for tissue information, and the comparison with phase values from the AIF was only performed in relative terms.

6.5. Relationship between concentration of contrast agent and phase/susceptibility

Because MRI CAs have inherently high magnetic susceptibility, the CA will cause an increase in susceptibility when present in human tissue or blood. The difference in susceptibility can be calculated if the molar susceptibility is known. At body temperature, the molar susceptibility for a Gd CA is typically 308 ppm/M [140], assumed to be independent of chelation. It should be noted that some degree of variability has been observed in phantom measurements, at body temperature [62] and at room temperature [119,141,142]. The change in susceptibility caused by the CA can be calculated as

$$\Delta\chi = \chi_{mol} \cdot C, \tag{49}$$

where C denotes the concentration of CA, and χ_{mol} is the molar susceptibility. This relationship was used to calculate the concentration levels reported in Papers IV and V. To illustrate how susceptibility and phase values vary in a typical dynamic series, during a CA passage, as in Papers III–V, values of susceptibility, as reported in Paper IV are given in Table 2 with the corresponding phase values if measured in a cylinder, calculated according to Eq. 46. For completeness, values per Eq. 46 are shown for tissues as well. However, cylinders are generally not a particularly good approximation for geometries corresponding to tissue regions. The phase tissue values should thus be interpreted only as approximate indications of the true phase levels.

Table 2. Examples of susceptibility and phase values at different levels of CA concentration. Concentration and susceptibility values are reported in Paper IV. Phase values are added for a cylinder oriented either parallel or perpendicular to the main magnetic field, measured at 3T with TE = 29 ms (as used in Papers IV and V).

Concentration (mM)	Susceptibility difference (ppm)	Phase (in radians) at TE = 29 ms at 3T Parallel cylinder	Phase (in radians) at TE = 29 ms at 3T Perpendicular cylinder
0.65 (Blood in CA steady state)	0.20	1.6	-0.78
0.026 (WM in CA steady state)	0.0079	0.062	-0.031
0.037 (GM in CA steady state)	0.011	0.088	-0.044
5.9 (Blood at max CA concentration)	1.8	14	-7.0
0.23 (WM at max CA concentration)	0.072	0.56	-0.28
0.33 (GM at max CA concentration)	0.10	0.80	-0.40

6.6. Phase-based information in blood

The use of phase information has been proposed for registration of both AIFs and VOFs to avoid problems associated with ΔR2*-based concentration estimates, such as a non-linear response to CA concentration in blood [126,131,143-146]. In the study described in Paper III, both AIFs and VOFs were obtained by using phase images, resulting in curves of the expected shape. When $\Delta\phi$ is known, the concentration of CA can, in principle, be estimated by a combination of Eqs. 43, 46 and 49, provided the angle between the blood vessel and the main magnetic field is known and that the blood vessel can be approximated by an infinite cylinder.

The strongest argument for using phase information for AIF and VOF measurements is probably the expected linear response of phase to CA concentration [62,131,144,147], because the linear relationship is important to obtain the correct shape of the curves. A higher SNR in phase-based compared with $\Delta R2^*$-based AIFs has also been shown [143,144,146], and when searching for AIFs with the correct shape and high SNR in the vicinity of the middle cerebral artery (MCA), phase information provides a larger number of useful AIF pixels [143]. It has also been shown that the response to the CA is independent of the haematocrit level (0 to 40% range) for phase data, in contrast to $\Delta R2^*$ data for which haematocrit levels influenced the shape of the ΔR2* versus concentration relationship [147].

There are, however, some problems associated with in vivo measurements, in which the measurement situation cannot be fully controlled, that need to be

addressed in order to find the true phase information. The main problem is that the measured phase depends not only on the concentration of CA, it is also affected by thermal noise, motion (including patient movements, breathing and pulsatile blood motion), temperature and instabilities of the MRI scanner (e.g. drift of the main magnetic field during the period of measurement) [145]. Examples of dynamic curves before any correction for these kinds of problems are shown in Fig. 14. For AIFs and VOFs, such effects have typically been accommodated by subtracting phase information from a pixel close to the AIF/VOF location exhibiting no obvious effect of the CA [131,145], and this apporach was also employed in Paper III. It can, however, be difficult to find a pixel without any CA effect, and a risk of subtracting phase information, which is, in fact, influenced by CA, exists. To avoid such effects, Garpebring et al. developed a sophisticated method to find a function to subtract from the AIF, based on voxels close to the AIF location [145].

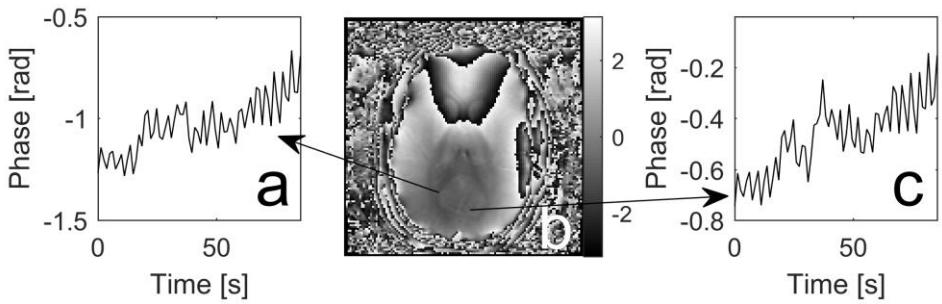

Figure 14. Visualisation of B_0 drift of the MRI scanner and other effects that influence the phase during a dynamic measurement. (a) Phase curve during the dynamic measurements from one WM pixel indicated by the arrow, (b) phase image without any additional post-processing, and (c) example of phase curve during the dynamic measurement from one GM pixel indicated by the arrow.

6.7. Dynamic contrast-enhanced phase mapping

Similar to observations in a blood vessel, the passage of CA in tissue can be followed using phase images, whereas the effects of geometry lead to a less predictable and more spatially variable phase evolution over time. In the literature, it is sometimes stated that the phase effect of CA in tissue will average to zero because of the randomised orientations of capillaries [62,67,143,148]. However, Conturo et al. [110] showed a net phase effect in the putamen in a dynamic study, after injection of a CA in baboons subjected to unilateral partial occlusion of the MCA. In the same study, the measured phase was plotted as a function of time after injection, and a relative measure of CBV was obtained as the AUC. In accordance with what was expected, the results indicated a reduced CBV in putamen in the ischemic hemisphere of the brain, affected by the MCA occlusion

[110]. Additionally, the study described in Paper III showed a net phase effect owing to CA in a small ROI in GM, giving $\Delta\phi$ versus time curves similar to those based on $\Delta R2^*$. Most likely, the non-zero net phase is caused by a bulk susceptibility effect from tissue structures of finite extension. It is also possible that the capillaries show a somewhat preferred direction, implying that the capillaries are not completely randomised and, furthermore, arterioles, venules, and sometimes even larger vessels might be present in tissue. Thus, $\Delta\phi$ values can be obtained in tissue as well, proportional to the concentration of CA. However, the proportionality factor is expected to be different for different tissue geometries and is generally not known. In Paper III, tissue curves and AIFs, based on phase images, were used to calculate CBF and MTT according to Eqs. 30 and 33, assuming that $\Delta\phi$ was proportional to concentration. Because the geometry factor was not considered, the estimated CBF values in Paper III were given in relative terms. It was, however, assumed that the geometry factor was similar for different subjects in corresponding regions, and when comparing the relative CBF values to ASL data, a good correlation was obtained for selected tissue regions.

7. Quantitative susceptibility mapping

7.1 Basic QSM concept

The task of reconstructing a spatial magnetic susceptibility distribution from MRI phase images is referred to as QSM. Hence, after the completion of phase unwrapping, conversion from phase to magnetic field and removal of background field contributions, the susceptibility can be estimated according to Eq. 44 or Eq. 45. Thus, a deconvolution of the magnetic field in a voxel, caused by sources around the voxel (estimated from phase images), and the unit dipole kernel must be accomplished. This constitutes a problem often referred to as an ill-posed inverse problem, because there are many spatially different susceptibility distributions that can result in the same magnetic field perturbation in a voxel. This is most easily understood by inspecting the convolution described in Fourier space (Eq. 45), where the Fourier transform of the susceptibility distribution is multiplied by the Fourier transform of the unit dipole. For k-space coordinates where $k_z^2/K^2 = 1/3$, the unit dipole is zero. Thus, information about the susceptibility is lost when the dipole is multiplied by the Fourier transform of the susceptibility distribution. The deconvolution, performed to obtain the susceptibility information can be described as[121-123,149]

$$\chi(r) = FT^{-1}\left[FT\left(\frac{\Delta B_z}{B_0}\right)\cdot \Pi\right], \tag{50}$$

where FT and FT^{-1} denote the forward and the inverse Fourier transform, respectively. Π is expressed as

$$\Pi = \frac{1}{\frac{1}{3} - \frac{k_z^2}{K^2}}. \tag{51}$$

Hence, when k_z^2/K^2 is close to 1/3, the value of Π is very high. If performing the deconvolution without considering these coordinates, the reconstructed susceptibility image will be dominated by streaking artefacts, and noise in the resulting susceptibility map will be amplified [123].

7.2 Measurement considerations

In contrast to the relative estimates of CA concentration described in Paper III, where phase images were used without any conversion to susceptibility, the work reported in Papers IV and V is based on the use of QSM for quantification of CA concentration. In practice, it is not entirely straightforward to obtain absolute values of susceptibility, because the susceptibility distribution returned by most QSM reconstruction algorithms comprise susceptibility maps in which the displayed values, χ_{QSM}, are shifted in relation to the true values, χ_{true} (i.e. $\chi_{QSM} = \chi_{true} + \chi_{Shift}$, where χ_{Shift} is a constant). Thus, to enable comparison, it is common to use either CSF or WM as a reference with known susceptibility. In the work described in Paper IV, CA concentration was obtained by comparing tissue susceptibility with CA to the tissue susceptibility without CA. Ideally, when susceptibilities at two different time points are compared, there would be no need to find a reference region, because χ_{Shift} would disappear in the subtraction of two different χ_{QSM} values. However, in practice, χ_{Shift} will differ among different time points because of instabilities in the MRI measurement (e.g. drift of the MRI scanner, shown in Fig. 14). Additionally, when using PDF and morphology-enabled dipole inversion (MEDI) to obtain susceptibility maps, as in Paper IV, information about the absolute level is lost in the post-processing. Thus, all susceptibility maps at different time points, corresponding to different CA concentrations, must be related to a reference region unaffected by CA. In a study by Lim et al. [150], susceptibility values in CSF were shown to vary considerably, and CSF was ruled out as a potential reference, with WM proposed as a better reference candidate. The large variations in CSF susceptibility estimates were assumed to be caused by pulsatile CSF flow and artefacts in QSM images, caused by the anisotropic susceptibility in WM. The artefact caused by WM anisotropy can be expected to be especially pronounced in CSF, because the ventricles are often surrounded by WM [151]. Despite these problems, CSF was chosen as a reference in Paper IV, because WM was not an option, owing to the need for a reference region that was unaffected by CA. However, problems with the use of CSF as a reference were indeed observed during the work with Paper IV. Thus, careful criteria were applied to optimise the selection of pixels to be included in the CSF reference ROI. The choice of CSF pixels, determined by different thresholds of the applied criteria, was shown to have a substantial impact on the estimated susceptibility values, represented by CBV variations in Paper IV, per Eq. 29. Recently, a method that might be beneficial in similar projects was presented, penalising large variations of susceptibility values in CSF to improve the procedure of finding a reliable reference region [151].

Obviously, PVEs would also be a potential problem in AIF registration in QSM images. However, studies comparing the effect of PVEs in magnitude- and phase-

based AIFs have indicated that PVEs will have less effect on the shape of the AIF, compared to magnitude AIFs [67,143,152]. Additionally, if the AIF is chosen in the vicinity of a vessel, there are more available voxels with the correct shape if the AIF is based on phase data instead of magnitude data [143]. Phase images are, however, not unaffected by PVEs, and the effect can be complicated for particular geometries. Xu et al. showed that the measured phase could vary substantially when measuring in a region containing a cylinder but with different PVEs, depending on the vessel diameter and orientation and the voxel dimensions [153]. Additionally, Haacke et al. showed that PVEs caused underestimated susceptibility in vessels perpendicular to B_0 when reconstructed by QSM [154].

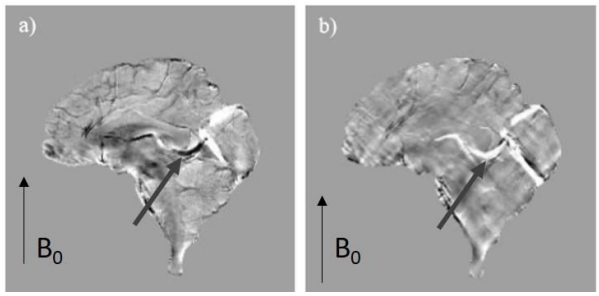

Figure 15. Images illustrating one of the benefits of using QSM instead of phase images. (a) Sagittal phase image and (b) QSM image of the same sagittal slice. The direction of the main magnetic field (B_0) is shown in the images. The grey arrow highlights how the phase differs along a vessel depending on the angle of the vessel relative the main magnetic field, while the QSM image shows similar values throughout the length of the vessel. (Credit: Emma Olsson)

One important issue to consider in the acquisition of data to be used for QSM calculations is the echo time TE. For phase images, the contrast, defined as the phase difference between two regions with different local magnetic field strengths, will increase linearly with TE [117]. However, for long TEs, the noise level is high and, to obtain the best CNR, the noise in the phase images must be considered [117]. The phase noise depends on the magnitude of the MRI signal and on the noise in the magnitude images. First, if the signal intensity is zero (or very low), every phase value between $-\pi$ and π is equally probable [155]. Secondly, for situations with high magnitude signal intensity, the noise will have a smaller effect on the phase value [155]. The noise standard deviation in phase images, σ_ϕ, for these two situations can be described per Eq. 52 [155,156]

$$\sigma_\phi = \begin{cases} \frac{\sigma}{S} \; if \; S \gg \sigma \\ \sqrt{\frac{\pi^2}{3}} if \; S = 0 \end{cases}. \tag{52}$$

Here, σ is the standard deviation of the noise in the real and imaginary parts of the MRI signal, which is equal to the noise standard deviations in magnitude image at regions with high intensities. S is the magnitude of the MRI signal. Thus, to obtain optimal CNR, TE should be chosen, such that TE ≈ T2* for the tissue of interest [117,118]. For studies of WM and GM at 3T, the optimal TE is thus approximately 30–40 ms [118], and the TE used in Papers III–V was 29 ms.

The noise in the phase images will obviously affect the noise in the reconstructed QSM images, and the standard deviation of the noise in estimated susceptibility, σ_χ, is given by [133]

$$\sigma_\chi = \frac{\kappa\sigma_\phi}{\gamma B_0 TE} = \frac{\alpha}{\gamma B_0 TE \cdot SNR_{mag}}. \quad (53)$$

Here, κ is a ratio of noise in the susceptibility image to the noise in the phase map, which will vary for different QSM algorithms, and SNR in the magnitude image is given by SNR_{mag}

7.3 Different QSM algorithms

Owing to the ill-posed nature of estimating susceptibility from magnetic field perturbations, many different methods exist, exploring different approaches to overcome the issue of missing information close to the magic angle in Fourier space.

The method referred to as calculation of susceptibility through multiple orientation sampling (COSMOS) [157] is often used as a gold standard or reference method for QSM measurements when different algorithms are compared or evaluated. In the COSMOS approach, the missing information at the magic angle is obtained by combining information from a series of measurements in which the object is positioned at different angles relative to the main magnetic field. Using this method, no regularisation is needed. However, owing to the uncomfortable and complicated measurement situation, the method is normally not applicable to a clinical setting.

Methods based on one measurement at a single orientation can be grouped into three different categories [132]. The first can be described as deconvolution by division in Fourier space, according to Eqs. 50 and 51. This is often referred to as thresholded k-space division (TKD) [123]. The problem with high values of Π in some regions is handled simply by replacing values above a certain threshold with a constant. The selected threshold is a compromise between obtaining the correct susceptibility values (higher threshold needed) and avoiding streaking artefacts (lower threshold needed). The second category of algorithms includes the use of

iterative methods to minimise the difference between the measured magnetic field and the magnetic field calculated from an estimated susceptibility distribution. Prior knowledge is typically included to obtain reliable solutions. One example from this group of algorithms is the MEDI approach [120,158], used in Papers IV and V, to be described in more detail below. The third category is similar to the second category in the sense that iterative methods are used to solve the same type of problem. In this category, the prior information is, however, only used for regularisation in the regions in Fourier space that closely correspond to the magic angle. For other parts of Fourier space, measured data remain unaffected. One example from this group is homogeneity-enabled incremental dipole inversion (HEIDI) [159], in which the Fourier space is divided in ill-conditioned and well-conditioned regions and an interim region.

In a comparison of different algorithms, applied to simulated data, phantom data and in vivo brain imaging, MEDI (used in Papers IV and V) performed well when compared to true values and values obtained via COSMOS [134]. Additionally, in a study by Deh et al., MEDI showed good repeatability in phantom measurements in a multicentre study including MRI scanners with several different field strengths and from different vendors [141]. However, in a multi-centre study in which different research groups were given the same data set, with the task to optimise their locally employed algorithm to create the best possible QSM images, the algorithms corresponding to the third category of algorithms generated the best results [160]. New methods are still being developed, and more accurate calculations in better agreement with the COSMOS results are expected in the future.

7.3.1 Morphology-enabled dipole inversion

In MEDI, morphological information from the magnitude image is used as prior information. Hence, the number of pixels defined as being close to an edge in the estimated susceptibility map, but not in the magnitude image, is minimised. Additionally, the difference between the magnetic field that would theoretically be created by the estimated susceptibility distribution and the local magnetic field actually measured must be equal to or smaller than the noise level. This can be expressed as follows [120,158,161]:

$$\min_{\chi} \|M\nabla\chi\|_1 \; subject\ to\ \|W(B_L - F_D\chi)\|_2^2 \leq \varepsilon. \tag{54}$$

M is a digital parameter used to assign the edges in the magnitude image. It is 1 where the gradient is large, corresponding to an edge, and 0 otherwise. ∇ denotes the 3D gradient operator, χ is the estimated susceptibility distribution, W is a weighting matrix accounting for noise variations over the image and B_L is the

measured local magnetic field corresponding to the susceptibility distribution inside the object. Additionally, ε is the noise level estimated from the magnitude images, and F_D is a matrix representation of the convolution with the unit dipole. If the regularisation parameter, λ, is chosen such that $\|W(B_L - F_D\chi\|_2^2 = \varepsilon$, the best solution for the susceptibility distribution, χ*, can be found [158]:

$$\chi^* = argmin_\chi \|M\nabla\chi\|_1 + \lambda \|W(B_L - F_D\chi)\|_2^2. \quad (55)$$

However, to reduce the impact of noise propagation in the inversion process, the complex function created by the field distributions can instead be estimated, according to Eq. 56 [162]:

$$\chi^* = argmin_\chi \|M\nabla\chi\|_1 + \lambda \left\|W\left(e^{iB_L} - e^{iF_D\chi}\right)\right\|_2^2. \quad (56)$$

To solve the minimisation problem, a cost function can be defined as

$$E = \|M\nabla\chi\|_1 + \lambda \left\|W\left(e^{iB_L} - e^{iF_D\chi}\right)\right\|_2^2. \quad (57)$$

Hence, the problem is solved by finding the susceptibility distribution corresponding to the case when the gradient, with respect to χ, of the cost function E is zero. This can be accomplished in an iterative process in which the susceptibility distribution is varied until the best solution is found [120,162].

7.4 Blood-volume estimation using QSM images

In Chapter 4, the principle of estimating CBV from susceptibility differences induced by the CA was described. In Paper IV, work with CBV estimation according to Eq. 29 was reported, using QSM by MEDI for quantification of magnetic susceptibility. It is, in principle, possible to collect separate images before and after the CA administration, similar to what was done to obtain CBV values from Bookend and VASO, as described in Paper I. However, in the study reported in Paper IV, phase data from GRE–EPI images acquired in a standard DSC–MRI experiment were used to enable the use of the whole dynamic measurement during the CA passage to improve the method of characterising reliable CSF reference pixels. As mentioned above, the repeatability of CBV values obtained from QSM data was dependent on the CSF reference, but when applying the optimised CSF reference region, the CBV repeatability was good, with intra-class correlation coefficient analyses showing r = 0.81 in WM and r =

0.91 in GM. Additionally, the optimised CSF reference generated absolute levels of CBV (2.93 ml/100 g in WM and 4.22 ml/100 g in GM) that were in reasonable agreement with previously published values, but with a somewhat lower GM-to-WM ratio (*cf.* 5.0 ml/100 g in GM and 2.6 ml/100 g in WM according to Leenders et al. [9]).

7.5 Dynamic contrast-enhanced QSM for perfusion imaging

Dynamic measurements of QSM can be used to obtain CA concentration estimates during the passage of CA, enabling application of the tracer dilution theory described in Chapter 3. Thus, apart from the data used for estimation of CA concentration, the method is very similar to DSC–MRI. In the work reported in Paper V, both ΔR2*-based and QSM-based perfusion parameters were estimated, similar to the study by Bonekamp et al. [163]. Despite the higher SNR in phase images reported by previous investigators [143,144,146], the observed CNR in QSM data was generally lower than for ΔR2* data both in Paper V and in Ref. [163]. However, a standard DSC–MRI pulse sequence, not optimised for QSM calculation, was used. CNR might be improved by using a 3D multi-TE GRE pulse sequence for QSM-based perfusion measurements, as proposed by Xu et al. [164]. However, no direct CNR comparison between QSM- and ΔR2*-based data was performed in that study [164]. When plotting perfusion estimates derived from QSM data as a function of perfusion estimates derived from ΔR2* data, a slope of 0.81 was found by Bonekamp et al. [163]. A similar value was found for data reported in Paper V by comparing CBF values in GM from the two different methods (see Fig. 16). Note, however, that the perfusion maps obtained by Bonekamp et al. [163] were rescaled to show the same CBF value in WM. Consequently, their comparison did not reflect results from different examinations, but instead compared the values within the CBF images.

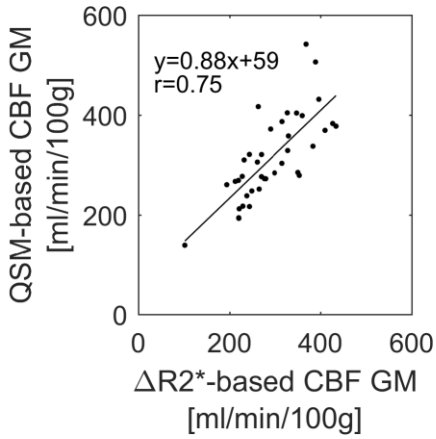

Figure 16. Scatter plot comparing CBF in GM estimated from $\Delta R2^*$ and QSM data (Paper V). Results from a linear regression analysis is also included.

7.6 QSM application for estimating oxygen metabolism

Perfusion is an indirect measure of tissue viability in the sense that it reflects the transport of oxygen and nutrients to the tissue of interest. Additional information of importance can be obtained by quantification of the actual oxygen consumption in the tissue. By combining information about CBF and OEF, $CMRO_2$ can be estimated [124].

$$CMRO_2 = OEF \cdot CBF \cdot C_a, \tag{58}$$

where C_a is the oxygen content in blood, usually given by a constant value. OEF can be estimated as $OEF = (Y_a - Y_v)/Y_a$, where Y_a and Y_v is the oxygen saturation level in an artery and vein, respectively. Because oxyhaemoglobin is diamagnetic and deoxyhaemoglobin is paramagnetic, the venous oxygen saturation level is associated with the magnetic susceptibility of the venous blood. The relationship can be described as [127]

$$\Delta\chi = \Delta\chi_{do} \cdot Hct \cdot (1 - Y). \tag{59}$$

$\Delta\chi$ refers to the difference in susceptibility between the vein and the surrounding tissue, Y is the oxygen saturation level for the blood vessel of interest, Hct is the haematocrit value, and $\Delta\chi_{do}$ is the difference in susceptibility between red blood cells without oxygen and fully oxygenated red blood cells.

By assuming that $Y_a = 1$, the relationships described above can be used to obtain information about global (i.e. whole-brain) oxygen consumption from phase images, translating phase to susceptibility per Eq. 46 [124,125,127,128] or from QSM images [165]. Information about the local oxygen saturation level in veins has also been obtained and presented as venograms in which the oxygen saturation was shown for different locations along the venous vessel tree [165]. Furthermore, pixel-wise estimation of $CMRO_2$ has been conducted, returning $CMRO_2$ maps comparable to those obtained by PET [166]. To enable estimation of local $CMRO_2$, coffee [167] and hyperventilation [168] have been used to alter CBF without changing $CMRO_2$. A method using small regions in which $CMRO_2$ and susceptibility of tissue without blood were assumed constant has also been presented [169].

8. Conclusions and future studies

The work reported in this doctoral thesis aimed at developing, improving, and evaluating different methods for quantification of perfusion using dynamic first pass contrast-enhanced MRI. In the studies reported in Papers I and II, approaches to calibrate conventional DSC–MRI data were employed, assuming that the shape of the AIF was correct and that no or only small effects of arterial delay, arterial dispersion, or deconvolution imperfections were present. Hence, the obtained values of CBF and CBV from the original DSC–MRI experiment were assumed to provide correct relative values. However, concerns about the shape of the AIF have been substantial in the literature, because a distorted shape would also affect relative CBF and absolute MTT estimates. In that sense, the results shown in Paper V are encouraging, because only a small difference in shape was observed for two CA quantification approaches. Whereas it is possible that both methods would show AIFs with distorted shapes compared to the true shape (e.g. caused by PVEs), it is unlikely that the effect on the shape would be the same for both phase-based and $\Delta R2^*$-based data. However, Paper V also indicated that only a slight difference in shape would affect the resulting perfusion estimates, but not substantially.

The results from all three calibration/correction approaches described in Papers I and II (i.e. Bookend, VASO, and prebolus) were encouraging in the sense that they returned absolute levels of CBF and CBV close to the reference method and/or literature values obtained by other modalities, such as PET. One interesting aspect of this is that Bookend and VASO were assumed to correct for all quantification issues related to DSC–MRI, whereas the prebolus correction is mainly expected to correct for PVEs in the AIF, and for effects of signal saturation and signal displacement. Thus, PVEs seem to be the main factor prohibiting perfusion quantification in absolute terms using DSC–MRI. For Bookend and VASO, the repeatability and the correlation with ASL results were not convincing, and further studies are required to evaluate the underlying reason for this, especially because other groups have shown results that are more promising. With respect to repeatability, the prebolus calibration approach seemed more promising. In particular, for the prebolus method, future studies including subjects with altered microcirculation comparted with normal volunteers would be of interest.

In the studies described in Papers III, IV, and V, the phase of the MRI signal was used to obtain information about CBF and CBV. Generally, good repeatability

(Paper IV) and good correlation with ASL data (Paper III) were seen. Paper III should, however, be viewed in light of the fact that it was compiled at a time when QSM reconstruction algorithms were not widely available. It should be regarded as a first step towards the use of phase information for perfusion assessment. Whereas promising and interesting at the time, the results of Paper III were only given in relative units and only for selected tissue regions. In future studies, it would be interesting to use CBV obtained from susceptibility information (Paper IV) for calibration, in the way reported for other CBV methods in Paper II. It is, however, crucial to establish a reliable way to perform the referencing (i.e. the shift of the QSM values) for QSM images obtained only at CA steady state. The method for referencing, described in Paper IV, should be further evaluated in other groups of subjects, because the method was developed and evaluated using the same datasets, and new algorithms for identification of reliable CSF susceptibility values are indeed promising in this context. For perfusion estimates based on dynamic QSM data, either using QSM-based AIFs only or based entirely on QSM data, a reliable CSF reference is also of utmost importance. Another important issue not accounted for in Papers III, IV, and V, is the potential manifestation of anisotropic susceptibility, particularly in WM, in the CA concentration quantification.

In conclusion, the results presented in this thesis indicate that PVEs in AIFs constitute a major issue in perfusion estimation using DSC–MRI data, and that calibration approaches tend to provide perfusion estimates of an expected level in absolute terms. Compared to QSM-based AIF registration, problems related to CA quantification using $\Delta R2^*$ appear to cause only minor to moderate deviations in the shape of an AIF that already has been judged to be acceptable by visual inspection. Even small distortions can, however, significantly but not substantially affect the resulting CBF and MTT values. Whereas substantial validation remains to be accomplished, a promising alternative method to $\Delta R2^*$ might be able to use QSM for CA quantification, if a reliable referencing approach can be established.

Acknowledgements

First, I would like to thank my main supervisor Ronnie Wirestam. Thank you for always being available for questions and interesting discussions and for always believing in me. Your knowledge in MR physics and your attention to details impresses me. I greatly appreciate working with someone who understands what I think even when my thoughts might sometimes not be entirely correct or a bit vaguely expressed.

I would also like to thank my co-supervisor Linda Knutsson. Your good mood and great knowledge about MRI perfusion measurements (among many other things) makes it a real pleasure to work with you. Thank you for all your help with my projects and for giving me insight into how the international research community works.

My co-supervisor Freddy Ståhlberg, thank you for all you help and for creating such a nice research environment. I am truly impressed by your organizing skills. Your long experience in MRI physics and your ability to see the greater picture has been an important asset to my work.

I am also thankful to all my co-authors for excellent collaboration: Karin Markenroth Block, Danielle van Westen, Matthias van Osch, André Ahlgren, and Yulia Surova.

I would also like to thank Peter van Zijl for you valuable thoughts about phase and QSM images.

Thank you to all colleagues at MSF, the MR physicists in Malmö and to all past and present members in the MR physics group in Lund. It is very rewarding to be surrounded by people with such impressing competence. Thank you for always being willing to help and for being such great people who makes MRI physics extra fun.

To Emma Olsson and Robin Kämpe, it was a pleasure to work with you in the field of phase and QSM images. Anna Lundberg, thank you for many rewarding discussions, both scientific and personal, I am truly happy to work with you.

A special thanks to Pernilla Peterson for being such a good friend, with whom I can also discuss work issues, and to Anna Rydhög, for great discussions, during times when it felt as if this doctoral thesis would never be written. Also, thank you Lena Trinh for many interesting talks about life as a PhD student and life in general.

I am also grateful for my friends; Linda, Michaela, Annika, Jennifer, Anna T, Sophie, Caroline, Challe, Emma, Maja, Christofer, Anna K, John, Nina, Bobbo,

CG, and Marina, with families, for always being the best of friends, who truly enrich my life.

To Emma Lindh and my parents-in-law with families; it is always a true joy to spend time with you. Thank you for many great moments and for always being interested in what I do.

To my parents, you are the best parents anyone can wish for. Thank you for always helping me with both big and small things and for making me feel that doing my best is always good enough. To my sister and to Rikard, Wilma, and Sam, you give my life so much joy. Spending time with you always makes me feel in a great mood.

An extra big thank you to Ted. Thank you for understanding when I have prioritized work before family and for always being my biggest supporter. Together we are the best team. Also, thank you Selma for being the greatest source of happiness and for making me put things in perspective

References

1. Knutsson L, Ståhlberg F, Wirestam R. Absolute quantification of perfusion using dynamic susceptibility contrast MRI: pitfalls and possibilities. Magn Reson Mater Phy 2010;23(1):1-21.
2. Baron JC. Perfusion thresholds in human cerebral ischemia: historical perspective and therapeutic implications. Cerebrovasc Dis 2001;11 Suppl 1:2-8.
3. McGehee BE, Maldjian JA, Burdette J. MR perfusion imaging in clinical neuroradiology. In: Barker PB, Golay X, Zaharchuk G, editors. Clinical perfusion MRI: techniques and applications. [Internet]. Cambridge, UK: Cambridge university press; 2013 [cited 2019 Jan 21]. Availablde from: Lund University Libraries
4. Umemura A, Suzuka T, Yamada K. Quantitative measurement of cerebral blood flow by ^{99m}Tc-HMPAO SPECT in acute ischaemic stroke: usefulness in determining therapeutic options. J Neurol Neurosurg Psychiatry 2000;69(4):472-478.
5. Betts JG, Desaix P, Johnson E, Johnson JE, Korol O, Kruse D, Poe B, Wise JA, Womble M, Young KA. Anatomy & Physiology [Internet]. Houston, Texas: OpenStax; 2013. [cited 2019 Jan 21]. Available from: https://openstax.org/details/books/anatomy-and-physiology
6. Buxton RB. Introduction to functional magnetic resonance imaging: principles and techniques [Internet]. Second edition. San Diego, USA: Cambridge university press; 2009 [cited 2019 Jan 21] Available from: Lund University Libraries
7. Fåhraeus R. The suspension stability of the blood. Physiological Reviews 1929;9(2):241-274.
8. Donahue MJ, Achten E, Cogswell PM, De Leeuw FE, Derdeyn CP, Dijkhuizen RM, Fan AP, Ghaznawi R, Heit JJ, Ikram MA, Jezzard P, Jordan LC, Jouvent E, Knutsson L, Leigh R, Liebeskind DS, Lin W, Okell TW, Qureshi AI, Stagg CJ, van Osch MJ, van Zijl PC, Watchmaker JM, Wintermark M, Wu O, Zaharchuk G, Zhou J, Hendrikse J. Consensus statement on current and emerging methods for the diagnosis and evaluation of cerebrovascular disease. J Cereb Blood Flow Metab 2018;38(9):1391-1417.
9. Leenders KL, Perani D, Lammertsma AA, Heather JD, Buckingham P, Healy MJ, Gibbs JM, Wise RJ, Hatazawa J, Herold S, Beaney RP, Brooks DJ, Spinks T, Rhodes C, Frackowiak RSJ, Jones T. Cerebral blood flow, blood volume and

oxygen utilization. Normal values and effect of age. Brain 1990;113 (Pt 1):27-47.

10. Lang EW, Mudaliar Y, Lagopoulos J, Dorsch N, Yam A, Griffith J, Mulvey J. A review of cerebral autoregulation: assessment and measurements. Australasian Anaesthesia 2005;161-172
11. Leigh R, Knutsson L, Zhou J, van Zijl PC. Imaging the physiological evolution of the ischemic penumbra in acute ischemic stroke. J Cereb Blood Flow Metab 2018;38(9):1500-1516.
12. Meier P, Zierler KL. On the theory of the indicator-dilution method for measurement of blood flow and volume. J Appl Physiol 1954;6(12):731-744.
13. Zaharchuk G. MR perfusion imaging in neurovascular disease. In: Barker PB, Golay X, Zaharchuk G, editors. Clinical perfusion MRI: techniques and applications. [Internet]. Cambridge, UK: Cambridge university press; 2013 [cited 2019 Jan 21]. Availablde from: Lund University Libraries
14. Albers GW, Thijs VN, Wechsler L, Kemp S, Schlaug G, Skalabrin E, Bammer R, Kakuda W, Lansberg MG, Shuaib A, Coplin W, Hamilton S, Moseley M, Marks MP. Magnetic resonance imaging profiles predict clinical response to early reperfusion: the diffusion and perfusion imaging evaluation for understanding stroke evolution (DEFUSE) study. Ann Neurol 2006;60(5):508-517.
15. Wu O, Koroshetz WJ, Østergaard L, Buonanno FS, Copen WA, Gonzalez RG, Rordorf G, Rosen BR, Schwamm LH, Weisskoff RM, Sorensen AG. Predicting tissue outcome in acute human cerebral ischemia using combined diffusion- and perfusion-weighted MR imaging. Stroke 2001;32(4):933-942.
16. The national institute of neurological disorders and stroke rt-PA stroke study group. Tissue plasminogen activator for acute ischemic stroke. N Engl J Med 1995;333(24):1581-1587.
17. Barajas RF, Cha S. MR perfusion imaging in oncology: neuro applications. In: Barker PB, Golay X, Zaharchuk G, editors. Clinical perfusion MRI: techniques and applications. [Internet]. Cambridge, UK: Cambridge university press; 2013 [cited 2019 Jan 21]. Availablde from: Lund University Libraries
18. Schuff N. MR perfusion imaging in neurodegenerative disease. In: Barker PB, Golay X, Zaharchuk G, editors. Clinical perfusion MRI: techniques and applications. [Internet]. Cambridge, UK: Cambridge university press; 2013 [cited 2019 Jan 21]. Availablde from: Lund University Libraries
19. Ellinger R, Kremser C, Schocke MF, Kolbitsch C, Griebel J, Felber SR, Aichner FT. The impact of peak saturation of the arterial input function on quantitative evaluation of dynamic susceptibility contrast-enhanced MR studies. J Comput Assist Tomogr 2000;24(6):942-948.
20. Knutsson L, Börjesson S, Larsson EM, Risberg J, Gustafson L, Passant U, Ståhlberg F, Wirestam R. Absolute quantification of cerebral blood flow in normal volunteers: correlation between Xe-133 SPECT and dynamic susceptibility contrast MRI. J Magn Reson Imaging 2007;26(4):913-920.

21. Srour JM, Shin W, Shah S, Sen A, Carroll TJ. SCALE-PWI: A pulse sequence for absolute quantitative cerebral perfusion imaging. J Cereb Blood Flow Metab 2011;31(5):1272-1282.

22. Dangouloff-Ros V, Deroulers C, Foissac F, Badoual M, Shotar E, Grévent D, Calmon R, Pagès M, Grill J, Dufour C, Blauwblomme T, Puget S, Zerah M, Sainte-Rose C, Brunelle F, Varlet P, Boddaert N. Arterial spin labeling to predict brain tumor grading in children: correlations between histopathologic vascular density and perfusion MR imaging. Radiology 2016;281(2):553-566.

23. Awasthi R, Rathore RK, Soni P, Sahoo P, Awasthi A, Husain N, Behari S, Singh RK, Pandey CM, Gupta RK. Discriminant analysis to classify glioma grading using dynamic contrast-enhanced MRI and immunohistochemical markers. Neuroradiology 2012;54(3):205-213.

24. Fountoulakis KN, Iacovides A, Gerasimou G, Fotiou F, Ioannidou C, Bascialla F, Grammaticos P, Kaprinis G. The relationship of regional cerebral blood flow with subtypes of major depression. Prog Neuro-psychopharmacol Biol Psychiatry 2004;28(3):537-546.

25. Ohgami H, Nagayama H, Akiyoshi J, Tsuchiyama K, Komaki S, Takaki H, Mori H. Contributing factors to changes of cerebral blood flow in major depressive disorder. J Affect Disord 2005;87(1):57-63.

26. Zierler KL. Theoretical basis of indicator-dilution methods for measuring flow and volume. Circ Res 1962;10(3):393-407.

27. Zierler KL. Equations for measuring blood flow by external monitoring of radioisotopes. Circ Res 1965;16:309-321.

28. Fieselmann A, Kowarschik M, Ganguly A, Hornegger J, Fahrig R. Deconvolution-based CT and MR brain perfusion measurement: theoretical model revisited and practical implementation details. Int J Biomed Imaging 2011;2011:1-20.

29. Wirestam R. Using contrast agents to obtain maps of regional perfusion and capillary wall permeability. Imaging Med 2012;4(4):423-442.

30. Ewing JR, Bonekamp D, Barker PB. Imaging of flow: basic principles. In: Barker PB, Golay X, Zaharchuk G, editors. Clinical perfusion MRI: techniques and applications. [Internet]. Cambridge, UK: Cambridge university press; 2013 [cited 2019 Jan 21]. Availablde from: Lund University Libraries

31. Catafau AM. Brain SPECT in clinical practice. Part I: perfusion. J Nucl Med 2001;42(2):259-271.

32. Wintermark M, Sesay M, Barbier E, Borbély K, Dillon WP, Eastwood JD, Glenn TC, Grandin CB, Pedraza S, Soustiel JF, Nariai T, Zaharchuk G, Caillé JM, Dousset V, Yonas H. Comparative overview of brain perfusion imaging techniques. Stroke 2005;36(9):e83-99.

33. O'Connor JPB, Tofts PS, Miles KA, Parkes LM, Thompson G, Jackson A. Dynamic contrast-enhanced imaging techniques: CT and MRI. Br J Radiol 2011;84 Spec No 2:S112-120.

34. Cosgrove D, Lassau N. Imaging of perfusion using ultrasound. Eur J Nucl Med Mol Imaging 2010;37 Suppl 1:S65-85.

35. Jahng GH, Li KL, Østergaard L, Calamante F. Perfusion magnetic resonance imaging: a comprehensive update on principles and techniques. Korean J Radiol 2014;15(5):554-577.

36. High WA, Ayers RA, Chandler J, Zito G, Cowper SE. Gadolinium is detectable within the tissue of patients with nephrogenic systemic fibrosis. J Am Acad Dermatol 2007;56(1):21-26.

37. Alsop DC, Detre JA, Golay X, Günther M, Hendrikse J, Hernandez-Garcia L, Lu H, MacIntosh BJ, Parkes LM, Smits M, van Osch MJ, Wang DJ, Wong EC, Zaharchuk G. Recommended implementation of arterial spin-labeled perfusion MRI for clinical applications: A consensus of the ISMRM perfusion study group and the European consortium for ASL in dementia. Magn Reson Med 2015;73(1):102-116.

38. Liu TT, Brown GG. Measurement of cerebral perfusion with arterial spin labeling: Part 1. Methods. J Int Neuropsychol Soc 2007;13(3):517-525.

39. Petcharunpaisan S, Ramalho J, Castillo M. Arterial spin labeling in neuroimaging. World J Radiol 2010;2(10):384-398.

40. Ferré JC, Bannier E, Raoult H, Mineur G, Carsin-Nicol B, Gauvrit JY. Arterial spin labeling (ASL) perfusion: techniques and clinical use. Diagn Interv Imaging 2013;94(12):1211-1223.

41. Petersen ET, Lim T, Golay X. Model-free arterial spin labeling quantification approach for perfusion MRI. Magn Reson Med 2006;55(2):219-232.

42. Alsop DC, Detre JA. Reduced transit-time sensitivity in noninvasive magnetic resonance imaging of human cerebral blood flow. J Cereb Blood Flow Metab 1996;16(6):1236-1249.

43. Wang J, Alsop DC, Li L, Listerud J, Gonzalez-At JB, Schnall MD, Detre JA. Comparison of quantitative perfusion imaging using arterial spin labeling at 1.5 and 4.0 Tesla. Magn Reson Med 2002;48(2):242-254.

44. Petersen ET, Mouridsen K, Golay X, all named co-authors of the QUASAR test-retest study. The QUASAR reproducibility study, Part II: Results from a multi-center arterial spin labeling test-retest study. Neuroimage 2010;49(1):104-113.

45. Shin W, Cashen TA, Horowitz SW, Sawlani R, Carroll TJ. Quantitative CBV measurement from static T1 changes in tissue and correction for intravascular water exchange. Magn Reson Med 2006;56(1):138-145.

46. Donahue KM, Weisskoff RM, Chesler DA, Kwong KK, Bogdanov AA, Mandeville JB Jr, Rosen BR. Improving MR quantification of regional blood volume with intravascular T1 contrast agents: accuracy, precision, and water exchange. Magn Reson Med 1996;36(6):858-867.

47. Hazlewood CF, Chang DC, Nichols BL, Woessner DE. Nuclear magnetic resonance transverse relaxation times of water protons in skeletal muscle. Biophys J 1974;14(8):583-606.

48. Shin W, Horowitz S, Ragin A, Chen Y, Walker M, Carroll TJ. Quantitative cerebral perfusion using dynamic susceptibility contrast MRI: evaluation of reproducibility and age- and gender-dependence with fully automatic image postprocessing algorithm. Magn Reson Med 2007;58(6):1232-1241.

49. Lu H, Law M, Johnson G, Ge Y, van Zijl PC, Helpern JA. Novel approach to the measurement of absolute cerebral blood volume using vascular-space-occupancy magnetic resonance imaging. Magn Reson Med 2005;54(6):1403-1411.

50. Uh J, Lewis-Amezcua K, Varghese R, Lu H. On the measurement of absolute cerebral blood volume (CBV) using vascular-space-occupancy (VASO) MRI. Magn Reson Med 2009;61(3):659-667.

51. Rempp KA, Brix G, Wenz F, Becker CR, Guckel F, Lorenz WJ. Quantification of regional cerebral blood flow and volume with dynamic susceptibility contrast-enhanced MR imaging. Radiology 1994;193(3):637-641.

52. Calamante F, Ahlgren A, van Osch MJ, Knutsson L. A novel approach to measure local cerebral haematocrit using MRI. J Cereb Blood Flow Metab 2016;36(4):768-780.

53. Ahlgren A, Wirestam R, Petersen ET, Ståhlberg F, Knutsson L. Perfusion quantification by model-free arterial spin labeling using nonlinear stochastic regularization deconvolution. Magn Reson Med 2013;70(5):1470-1480.

54. Calamante F. Bolus dispersion issues related to the quantification of perfusion MRI data. J Magn Reson Imaging 2005;22(6):718-722.

55. Østergaard L, Weisskoff RM, Chesler DA, Gyldensted C, Rosen BR. High resolution measurement of cerebral blood flow using intravascular tracer bolus passages. Part I: Mathematical approach and statistical analysis. Magn Reson Med 1996;36(5):715-725.

56. Knutsson L, Ståhlberg F, Wirestam R. Aspects on the accuracy of cerebral perfusion parameters obtained by dynamic susceptibility contrast MRI: a simulation study. Magn Reson Imaging 2004;22(6):789-798.

57. van Osch MJ, Vonken EJ, Wu O, Viergever MA, van der Grond J, Bakker CJ. Model of the human vasculature for studying the influence of contrast injection speed on cerebral perfusion MRI. Magn Reson Med 2003;50(3):614-622.

58. Boxerman JL, Hamberg LM, Rosen BR, Weisskoff RM. MR contrast due to intravascular magnetic susceptibility perturbations. Magn Reson Med 1995;34(4):555-566.

59. Dennie J, Mandeville JB, Boxerman JL, Packard SD, Rosen BR, Weisskoff RM. NMR imaging of changes in vascular morphology due to tumor angiogenesis. Magn Reson Med 1998;40(6):793-799.

60. Willats L, Calamante F. The 39 steps: evading error and deciphering the secrets for accurate dynamic susceptibility contrast MRI. NMR Biomed 2013;26(8):913-931.

61. Kjølby BF, Østergaard L, Kiselev VG. Theoretical model of intravascular paramagnetic tracers effect on tissue relaxation. Magn Reson Med 2006;56(1):187-197.

62. van Osch MJ, Vonken EJ, Viergever MA, van der Grond J, Bakker CJ. Measuring the arterial input function with gradient echo sequences. Magn Reson Med 2003;49(6):1067-1076.

63. Akbudak E, Kotys M, Conturo T. Quadraticity and hematocrit dependence of ΔR2* AIF signals at 3T: a blood phantom study under physiologic conditions. Syllabus of the ISMRM workshop on quantitative cerebral perfusion imaging using MRI; a technical perspective, Venice, Italy;2004.p 10-11.

64. Morell A, Lennmyr F, Jonsson O, Tovedal T, Pettersson J, Bergquist J, Zemgulis V, Einarsson GM, Thelin S, Ahlström H, Bjørnerud A. Influence of blood/tissue differences in contrast agent relaxivity on tracer-based MR perfusion measurements. Magn Reson Mater Phy 2015;28(2):135-147.

65. Rausch M, Scheffler K, Rudin M, Radü EW. Analysis of input functions from different arterial branches with gamma variate functions and cluster analysis for quantitative blood volume measurements. Magn Reson Imaging 2000;18(10):1235-1243.

66. Kjølby BF, Mikkelsen IK, Pedersen M, Østergaard L, Kiselev VG. Analysis of partial volume effects on arterial input functions using gradient echo: a simulation study. Magn Reson Med 2009;61(6):1300-1309.

67. van Osch MJ, Vonken EJ, Bakker CJ, Viergever MA. Correcting partial volume artifacts of the arterial input function in quantitative cerebral perfusion MRI. Magn Reson Med 2001;45(3):477-485.

68. Chen JJ, Smith MR, Frayne R. The impact of partial-volume effects in dynamic susceptibility contrast magnetic resonance perfusion imaging. J Magn Reson Imaging 2005;22(3):390-399.

69. Calamante F. Arterial input function in perfusion MRI: a comprehensive review. Prog Nucl Magn Reson Spectrosc 2013;74:1-32.

70. Quarles CC, Gochberg DF, Gore JC, Yankeelov TE. A theoretical framework to model DSC-MRI data acquired in the presence of contrast agent extravasation. Phys Med Biol 2009;54(19):5749-5766.

71. Bjørnerud A, Sorensen AG, Mouridsen K, Emblem KE. T1- and T2*-dominant extravasation correction in DSC-MRI: part I-theoretical considerations and implications for assessment of tumor hemodynamic properties. J Cereb Blood Flow Metab 2011;31(10):2041-2053.

72. Boxerman JL, Schmainda KM, Weisskoff RM. Relative cerebral blood volume maps corrected for contrast agent extravasation significantly correlate with glioma tumor grade, whereas uncorrected maps do not. AJNR Am J Neuroradiol 2006;27(4):859-867.

73. Emblem KE, Bjørnerud A, Mouridsen K, Borra RJ, Batchelor TT, Jain RK, Sorensen AG. T1-and T2*-dominant extravasation correction in DSC-MRI: Part

II—predicting patient outcome after a single dose of cediranib in recurrent glioblastoma patients. J Cereb Blood Flow Metab 2011;31(10):2054-2064.

74. Haselhorst R, Kappos L, Bilecen D, Scheffler K, Möri D, Radü EW, Seelig J. Dynamic susceptibility contrast MR imaging of plaque development in multiple sclerosis: application of an extended blood-brain barrier leakage correction. J Magn Reson Imaging 2000;11(5):495-505.

75. Vonken EP, van Osch MJ, Bakker CJ, Viergever MA. Simultaneous quantitative cerebral perfusion and Gd-DTPA extravasation measurement with dual-echo dynamic susceptibility contrast MRI. Magn Reson Med 2000;43(6):820-827.

76. Bjørnerud A, Emblem KE. A fully automated method for quantitative cerebral hemodynamic analysis using DSC-MRI. J Cereb Blood Flow Metab 2010;30(5):1066-1078.

77. Calamante F, Gadian DG, Connelly A. Quantification of bolus-tracking MRI: Improved characterization of the tissue residue function using Tikhonov regularization. Magn Reson Med 2003;50(6):1237-1247.

78. Wirestam R, Andersson L, Østergaard L, Bolling M, Aunola JP, Lindgren A, Geijer B, Holtås S, Ståhlberg F. Assessment of regional cerebral blood flow by dynamic susceptibility contrast MRI using different deconvolution techniques. Magn Reson Med 2000;43(5):691-700.

79. Wu O, Østergaard L, Weisskoff RM, Benner T, Rosen BR, Sorensen AG. Tracer arrival timing-insensitive technique for estimating flow in MR perfusion-weighted imaging using singular value decomposition with a block-circulant deconvolution matrix. Magn Reson Med 2003;50(1):164-174.

80. Zanderigo F, Bertoldo A, Pillonetto G, Cobelli C. Nonlinear stochastic regularization to characterize tissue residue function in bolus-tracking MRI: assessment and comparison with SVD, block-circulant SVD, and Tikhonov. IEEE Trans Biomed Eng 2009;56(5):1287-1297.

81. Digernes I, Bjørnerud A, Vatnehol SAS, Løvland G, Courivaud F, Vik-Mo E, Meling TR, Emblem KE. A theoretical framework for determining cerebral vascular function and heterogeneity from dynamic susceptibility contrast MRI. J Cereb Blood Flow Metab 2017;37(6):2237-2248.

82. Jespersen SN, Østergaard L. The roles of cerebral blood flow, capillary transit time heterogeneity, and oxygen tension in brain oxygenation and metabolism. J Cereb Blood Flow Metab 2012;32(2):264-277.

83. Mouridsen K, Hansen MB, Østergaard L, Jespersen SN. Reliable estimation of capillary transit time distributions using DSC-MRI. J Cereb Blood Flow Metab 2014;34(9):1511-1521.

84. Østergaard L, Chesler DA, Weisskoff RM, Sorensen AG, Rosen BR. Modeling cerebral blood flow and flow heterogeneity from magnetic resonance residue data. J Cereb Blood Flow Metab 1999;19(6):690-699.

85. Calamante F, Mørup M, Hansen LK. Defining a local arterial input function for perfusion MRI using independent component analysis. Magn Reson Med 2004;52(4):789-797.

86. Knutsson L, Larsson EM, Thilmann O, Ståhlberg F, Wirestam R. Calculation of cerebral perfusion parameters using regional arterial input functions identified by factor analysis. J Magn Reson Imaging 2006;23(4):444-453.

87. Willats L, Christensen S, Ma HK, Donnan GA, Connelly A, Calamante F. Validating a local arterial input function method for improved perfusion quantification in stroke. J Cereb Blood Flow Metab 2011;31(11):2189-2198.

88. Calamante F, Gadian DG, Connelly A. Delay and dispersion effects in dynamic susceptibility contrast MRI: simulations using singular value decomposition. Magn Reson Med 2000;44(3):466-473.

89. Willats L, Connelly A, Calamante F. Improved deconvolution of perfusion MRI data in the presence of bolus delay and dispersion. Magn Reson Med 2006;56(1):146-156.

90. Willats L, Connelly A, Calamante F. Minimising the effects of bolus dispersion in bolus-tracking MRI. NMR Biomed 2008;21(10):1126-1137.

91. Engvall C, Ryding E, Wirestam R, Holtås S, Ljunggren K, Ohlsson T, Reinstrup P. Human cerebral blood volume (CBV) measured by dynamic susceptibility contrast MRI and ^{99m}Tc-RBC SPECT. J Neurosurg Anesthesiol 2008;20(1):41-44.

92. Østergaard L, Sorensen AG, Kwong KK, Weisskoff RM, Gyldensted C, Rosen BR. High resolution measurement of cerebral blood flow using intravascular tracer bolus passages. Part II: Experimental comparison and preliminary results. Magn Reson Med 1996;36(5):726-736.

93. Østergaard L, Johannsen P, Høst-Poulsen P, Vestergaard-Poulsen P, Asboe H, Gee AD, Hansen SB, Cold GE, Gjedde A, Gyldensted C. Cerebral blood flow measurements by magnetic resonance imaging bolus tracking: comparison with [^{15}O]H_2O positron emission tomography in humans. J Cereb Blood Flow Metab 1998;18(9):935-940.

94. Mukherjee P, Kang HC, Videen TO, McKinstry RC, Powers WJ, Derdeyn CP. Measurement of cerebral blood flow in chronic carotid occlusive disease: comparison of dynamic susceptibility contrast perfusion MR imaging with positron emission tomography. AJNR Am J Neuroradiol 2003;24(5):862-871.

95. Kaneko K, Kuwabara Y, Mihara F, Yoshiura T, Nakagawa M, Tanaka A, Sasaki M, Koga H, Hayashi K, Honda H. Validation of the CBF, CBV, and MTT values by perfusion MRI in chronic occlusive cerebrovascular disease: a comparison with ^{15}O-PET. Acad Radiol 2004;11(5):489-497.

96. Knutsson L, Lindgren E, Ahlgren A, van Osch MJ, Markenroth Bloch K, Surova Y, Ståhlberg F, van Westen D, Wirestam R. Reduction of arterial partial volume effects for improved absolute quantification of DSC-MRI perfusion estimates: comparison between tail scaling and prebolus administration. J Magn Reson imaging 2015;41(4):903-908.

97. Knutsson L, Xu X, Ståhlberg F, Barker PB, Lind E, Sundgren PC, van Zijl PCM, Wirestam R. Dynamic susceptibility contrast MRI at 7 T: tail-scaling analysis and inferences about field strength dependence. Tomography 2017;3(2):74-78.

98. Crane DE, Donahue MJ, Chappell MA, Sideso E, Handa A, Kennedy J, Jezzard P, MacIntosh BJ. Evaluating quantitative approaches to dynamic susceptibility contrast MRI among carotid endarterectomy patients. J Magn Reson Imaging 2013;37(4):936-943.

99. Vakil P, Lee JJ, Mouannes-Srour JJ, Derdeyn CP, Carroll TJ. Cerebrovascular occlusive disease: quantitative cerebral blood flow using dynamic susceptibility contrast MR imaging correlates with quantitative $H_2[^{15}O]$ PET. Radiology 2013;266(3):879-886.

100. D'Ortenzio RM, Hojjat SP, Vitorino R, Cantrell CG, Lee L, Feinstein A, O'Connor P, Carroll TJ, Aviv RI. Comparison of quantitative cerebral blood flow measurements performed by Bookend dynamic susceptibility contrast and arterial spin-labeling MRI in relapsing-remitting multiple sclerosis. AJNR Am J Neuroradiol 2016;37(12):2265-2272.

101. Uh J, Lin AL, Lee K, Liu P, Fox P, Lu H. Validation of VASO cerebral blood volume measurement with positron emission tomography. Magn Reson Med 2011;65(3):744-749.

102. Zaharchuk G, Straka M, Marks MP, Albers GW, Moseley ME, Bammer R. Combined arterial spin label and dynamic susceptibility contrast measurement of cerebral blood flow. Magn Reson Med 2010;63(6):1548-1556.

103. Bonekamp D, Mahaveer D, Barker P. Quantitative cerebral blood flow in dynamic susceptibility contrast MRI using total cerebral flow from phase-contrast MRA. Magn Reson Med 2011;66(1):57-66.

104. Haacke EM, Xu Y, Cheng YC, Reichenbach JR. Susceptibility weighted imaging (SWI). Magn Reson Med 2004;52(3):612-618.

105. Reichenbach JR, Venkatesan R, Schillinger DJ, Kido DK, Haacke EM. Small vessels in the human brain: MR venography with deoxyhemoglobin as an intrinsic contrast agent. Radiology 1997;204(1):272-277.

106. Abduljalil AM, Schmalbrock P, Novak V, Chakeres DW. Enhanced gray and white matter contrast of phase susceptibility-weighted images in ultra-high-field magnetic resonance imaging. J Magn Reson Imaging 2003;18(3):284-290.

107. Duyn JH, van Gelderen P, Li TQ, de Zwart JA, Koretsky AP, Fukunaga M. High-field MRI of brain cortical substructure based on signal phase. Proc Natl Acad Sci U S A 2007;104(28):11796-11801.

108. Rauscher A, Sedlacik J, Barth M, Mentzel HJ, Reichenbach JR. Magnetic susceptibility-weighted MR phase imaging of the human brain. AJNR Am J Neuroradiol 2005;26(4):736-742.

109. Reichenbach JR, Schweser F, Serres B, Deistung A. Quantitative susceptibility mapping: concepts and applications. Clin Neuroradiol 2015;25 Suppl 2:225-230.

110. Conturo TE, Barker PB, Mathews VP, Monsein LH, Bryan RN. MR imaging of cerebral perfusion by phase-angle reconstruction of bolus paramagnetic-induced frequency shifts. Magn Reson Med 1992;27(2):375-390.

111. Bryant DJ, Payne JA, Firmin DN, Longmore DB. Measurement of flow with NMR imaging using a gradient pulse and phase difference technique. J Comput Assist Tomogr 1984;8(4):588-593.

112. Lotz J, Meier C, Leppert A, Galanski M. Cardiovascular flow measurement with phase-contrast MR imaging: basic facts and implementation. Radiographics 2002;22(3):651-671.

113. Ståhlberg F, Mogelvang J, Thomsen C, Nordell B, Stubgaard M, Ericsson A, Sperber G, Greitz D, Larsson H, Henriksen O, Persson B. A method for MR quantification of flow velocities in blood and CSF using interleaved gradient-echo pulse sequences. Magn Reson Imaging 1989;7(6):655-667.

114. Haacke M BR, Thompson M, Venkatesan R. Magnetic resonance imaging: physical principles and sequence design - Chapter 25 Magnetic Properties of Tissues: Theory and Measurement. 1999.

115. Liu C. Susceptibility tensor imaging. Magn Reson Med 2010;63(6):1471-1477.

116. Li W, Wu B, Avram AV, Liu C. Magnetic susceptibility anisotropy of human brain in vivo and its molecular underpinnings. Neuroimage 2012;59(3):2088-2097.

117. Schweser F, Deistung A, Reichenbach JR. Foundations of MRI phase imaging and processing for Quantitative Susceptibility Mapping (QSM). Z Med Phys 2016;26(1):6-34.

118. Liu C, Li W, Tong KA, Yeom KW, Kuzminski S. Susceptibility-weighted imaging and quantitative susceptibility mapping in the brain. J Magn Reson Imaging 2015;42(1):23-41.

119. de Rochefort L, Brown R, Prince MR, Wang Y. Quantitative MR susceptibility mapping using piece-wise constant regularized inversion of the magnetic field. Magn Reson Med 2008;60(4):1003-1009.

120. Liu J, Liu T, de Rochefort L, Ledoux J, Khalidov I, Chen W, Tsiouris AJ, Wisnieff C, Spincemaille P, Prince MR, Wang Y. Morphology enabled dipole inversion for quantitative susceptibility mapping using structural consistency between the magnitude image and the susceptibility map. Neuroimage 2012;59(3):2560-2568.

121. Marques J, Bowtell R. Application of a Fourier-based method for rapid calculation of field inhomogeneity due to spatial variation of magnetic susceptibility. Concepts in Magnetic Resonance Part B: Magnetic Resonance Engineering 2005;25B(1):65-78.

122. Salomir R, de Senneville BD, Moonen CT. A fast calculation method for magnetic field inhomogeneity due to an arbitrary distribution of bulk susceptibility. Concepts in Magnetic Resonance Part B: Magnetic Resonance Engineering 2003;19B(1):26-34.

123. Shmueli K, de Zwart JA, van Gelderen P, Li TQ, Dodd SJ, Duyn JH. Magnetic susceptibility mapping of brain tissue in vivo using MRI phase data. Magn Reson Med 2009;62(6):1510-1522.

124. Fan AP, Benner T, Bolar DS, Rosen BR, Adalsteinsson E. Phase-based regional oxygen metabolism (PROM) using MRI. Magn Reson Med 2012;67(3):669-678.

125. Fernández-Seara MA, Techawiboonwong A, Detre JA, Wehrli FW. MR susceptometry for measuring global brain oxygen extraction. Magn Reson Med 2006;55(5):967-973.

126. Foottit C, Cron GO, Hogan MJ, Nguyen TB, Cameron I. Determination of the venous output function from MR signal phase: feasibility for quantitative DCE-MRI in human brain. Magn Reson Med 2010;63(3):772-781.

127. Haacke EM, Lai S, Reichenbach JR, Kuppusamy K, Hoogenraad FG, Takeichi H, Lin W. In vivo measurement of blood oxygen saturation using magnetic resonance imaging: a direct validation of the blood oxygen level-dependent concept in functional brain imaging. Hum Brain Mapp 1997;5(5):341-346.

128. Kämpe R, Lind E, Ståhlberg F, van Westen D, Knutsson L, Wirestam R. Quantification of normal cerebral oxygen extraction and oxygen metabolism by phase-based MRI susceptometry: evaluation of repeatability using two different imaging protocols. Clin Physiol Funct Imaging 2017;37(2):211-220.

129. Li C, Langham MC, Epstein CL, Magland JF, Wu J, Gee J, Wehrli FW. Accuracy of the cylinder approximation for susceptometric measurement of intravascular oxygen saturation. Magn Reson Med 2012;67(3):808-813.

130. Cusack R, Papadakis N. New robust 3-D phase unwrapping algorithms: application to magnetic field mapping and undistorting echoplanar images. Neuroimage 2002;16(3 Pt 1):754-764.

131. Akbudak E, Conturo TE. Arterial input functions from MR phase imaging. Magn Reson Med 1996;36(6):809-815.

132. Deistung A, Schweser F, Reichenbach JR. Overview of quantitative susceptibility mapping. NMR Biomed 2017;30(4):e3569.

133. Haacke EM, Liu S, Buch S, Zheng W, Wu D, Ye Y. Quantitative susceptibility mapping: current status and future directions. Magn Reson Imaging 2015;33(1):1-25.

134. Wang Y, Liu T. Quantitative susceptibility mapping (QSM): Decoding MRI data for a tissue magnetic biomarker. Magn Reson Med 2015;73(1):82-101.

135. Neelavalli J, Cheng YC, Jiang J, Haacke EM. Removing background phase variations in susceptibility-weighted imaging using a fast, forward-field calculation. J Magn Reson Imaging 2009;29(4):937-948.

136. Schweser F, Deistung A, Lehr BW, Reichenbach JR. Quantitative imaging of intrinsic magnetic tissue properties using MRI signal phase: an approach to in vivo brain iron metabolism? Neuroimage 2011;54(4):2789-2807.

137. Zhou D, Liu T, Spincemaille P, Wang Y. Background field removal by solving the Laplacian boundary value problem. NMR Biomed 2014;27(3):312-319.

138. Liu T, Khalidov I, de Rochefort L, Spincemaille P, Liu J, Tsiouris AJ, Wang Y. A novel background field removal method for MRI using projection onto dipole fields (PDF). NMR Biomed 2011;24(9):1129-1136.

139. Schweser F, Robinson SD, de Rochefort L, Li W, Bredies K. An illustrated comparison of processing methods for phase MRI and QSM: removal of background field contributions from sources outside the region of interest. NMR Biomed 2017;30(4):e3604.

140. de Rochefort L, Nguyen T, Brown R, Spincemaille P, Choi G, Weinsaft J, Prince MR, Wang Y. In vivo quantification of contrast agent concentration using the induced magnetic field for time-resolved arterial input function measurement with MRI. Med phys 2008;35(12):5328-5339.

141. Deh K, Kawaji K, Bulk M, Van Der Weerd L, Lind E, Spincemaille P, McCabe Gillen K, Van Auderkerke J, Wang Y, Nguyen TD. Multicenter reproducibility of quantitative susceptibility mapping in a gadolinium phantom using MEDI+0 automatic zero referencing. Magn Reson Med 2019;81(2):1229-1236.

142. Olsson E, Wirestam R, Lind E. MRI-Based Quantification of Magnetic Susceptibility in Gel Phantoms: Assessment of Measurement and Calculation Accuracy. Radiol Res Pract 2018;2018:6709525.

143. Bleeker EJ, van Buchem MA, Webb AG, van Osch MJ. Phase-based arterial input function measurements for dynamic susceptibility contrast MRI. Magn Reson Med 2010;64(2):358-368.

144. Conturo TE, Akbudak E, Kotys MS, Chen ML, Chun SJ, Hsu RM, Sweeney CC, Markham J. Arterial input functions for dynamic susceptibility contrast MRI: requirements and signal options. J Magn Reson Imaging 2005;22(6):697-703.

145. Garpebring A, Wirestam R, Yu J, Asklund T, Karlsson M. Phase-based arterial input functions in humans applied to dynamic contrast-enhanced MRI: potential usefulness and limitations. Magn Reson Mater Phy 2011;24(4):233-245.

146. Kotys MS, Akbudak E, Markham J, Conturo TE. Precision, signal-to-noise ratio, and dose optimization of magnitude and phase arterial input functions in dynamic susceptibility contrast MRI. J Magn Reson Imaging 2007;25(3):598-611.

147. Akbudak E, Hsu RM, Li Y, Conturo TE. ΔR^* and $\Delta\varphi$ contrast agent perfusion effects in blood: quantitation and linearity assessment. In: Proceedings of the 6th scientific meeting, International Society for Magnetic Resonance in medicine, Sydney, Australia; 1998:p 1197.

148. Marques JP, Bowtell RW. Using forward calculations of the magnetic field perturbation due to a realistic vascular model to explore the BOLD effect. NMR Biomed 2008;21(6):553-565.

149. Haacke EM, Cheng NY, House MJ, Liu Q, Neelavalli J, Ogg RJ, Khan A, Ayaz M, Kirsch W, Obenaus A. Imaging iron stores in the brain using magnetic resonance imaging. Magn Reson Imaging 2005;23(1):1-25.

150. Lim IA, Faria AV, Li X, Hsu JT, Airan RD, Mori S, van Zijl PC. Human brain atlas for automated region of interest selection in quantitative susceptibility mapping: application to determine iron content in deep gray matter structures. Neuroimage 2013;82:449-469.

151. Liu Z, Spincemaille P, Yao Y, Zhang Y, Wang Y. MEDI+0: Morphology enabled dipole inversion with automatic uniform cerebrospinal fluid zero reference for quantitative susceptibility mapping. Magn Reson Med 2018;79(5):2795-2803.

152. Cron GO, Wallace JC, Stevens WD, Fortin T, Pappas BA, Wilkins RC, Kelcz F, Santyr GE. A comparison of T2*-weighted magnitude and phase imaging for measuring the arterial input function in the rat aorta following intravenous injection of gadolinium contrast agent. Magn Reson Imaging 2005;23(5):619-627.

153. Xu Y, Haacke EM. The role of voxel aspect ratio in determining apparent vascular phase behavior in susceptibility weighted imaging. Magn Reson Imaging 2006;24(2):155-160.

154. Haacke EM, Tang J, Neelavalli J, Cheng YC. Susceptibility mapping as a means to visualize veins and quantify oxygen saturation. J Magn Reson Imaging 2010;32(3):663-676.

155. Gudbjartsson H, Patz S. The Rician distribution of noisy MRI data. Magn Reson Med 1995;34(6):910-914.

156. Andersen AH. On the Rician distribution of noisy MRI data. Magn Reson Med 1996;36(2):331-333.

157. Liu T, Spincemaille P, de Rochefort L, Kressler B, Wang Y. Calculation of susceptibility through multiple orientation sampling (COSMOS): a method for conditioning the inverse problem from measured magnetic field map to susceptibility source image in MRI. Magn Reson Med 2009;61(1):196-204.

158. Liu T, Liu J, de Rochefort L, Spincemaille P, Khalidov I, Ledoux JR, Wang Y. Morphology enabled dipole inversion (MEDI) from a single-angle acquisition: comparison with COSMOS in human brain imaging. Magn Reson Med 2011;66(3):777-783.

159. Schweser F, Sommer K, Deistung A, Reichenbach JR. Quantitative susceptibility mapping for investigating subtle susceptibility variations in the human brain. Neuroimage 2012;62(3):2083-2100.

160. Langkammer C, Schweser F, Shmueli K, Kames C, Li X, Guo L, Milovic C, Kim J, Wei H, Bredies K, Buch S, Guo Y, Liu Z, Meineke J, Rauscher A, Marques JP, Bilgic B. Quantitative susceptibility mapping: Report from the 2016 reconstruction challenge. Magn Reson Med 2018;79(3):1661-1673.

161. de Rochefort L, Liu T, Kressler B, Liu J, Spincemaille P, Lebon V, Wu J, Wang Y. Quantitative susceptibility map reconstruction from MR phase data using bayesian regularization: validation and application to brain imaging. Magn Reson Med 2010;63(1):194-206.

162. Liu T, Wisnieff C, Lou M, Chen W, Spincemaille P, Wang Y. Nonlinear formulation of the magnetic field to source relationship for robust quantitative susceptibility mapping. Magn Reson Med 2013;69(2):467-476.

163. Bonekamp D, Barker PB, Leigh R, van Zijl PC, Li X. Susceptibility-based analysis of dynamic gadolinium bolus perfusion MRI. Magn Reson Med 2015;73(2):544-554.

164. Xu B, Spincemaille P, Liu T, Prince MR, Dutruel S, Gupta A, Thimmappa ND, Wang Y. Quantification of cerebral perfusion using dynamic quantitative susceptibility mapping. Magn Reson Med 2015;73(4):1540-1548.

165. Fan AP, Bilgic B, Gagnon L, Witzel T, Bhat H, Rosen BR, Adalsteinsson E. Quantitative oxygenation venography from MRI phase. Magn Reson Med 2014;72(1):149-159.

166. Kudo K, Liu T, Murakami T, Goodwin J, Uwano I, Yamashita F, Higuchi S, Wang Y, Ogasawara K, Ogawa A, Sasaki M. Oxygen extraction fraction measurement using quantitative susceptibility mapping: Comparison with positron emission tomography. J Cereb Blood Flow Metab 2016;36(8):1424-1433.

167. Zhang J, Liu T, Gupta A, Spincemaille P, Nguyen TD, Wang Y. Quantitative mapping of cerebral metabolic rate of oxygen (CMRO2) using quantitative susceptibility mapping (QSM). Magn Reson Med 2015;74(4):945-952.

168. Zhang J, Zhou D, Nguyen TD, Spincemaille P, Gupta A, Wang Y. Cerebral metabolic rate of oxygen (CMRO2) mapping with hyperventilation challenge using quantitative susceptibility mapping (QSM). Magn Reson Med 2017;77(5):1762-1773.

169. Zhang J, Cho J, Zhou D, Nguyen TD, Spincemaille P, Gupta A, Wang Y. Quantitative susceptibility mapping-based cerebral metabolic rate of oxygen mapping with minimum local variance. Magn Reson Med 2018;79(1):172-179.

Printed by Media-Tryck, Lund 2019 NORDIC SWAN ECOLABEL 3041 0903

Department of Medical Radiation Physics
Faculty of Science

ISBN 978-91-7753-972-8